RESEARCH ARTICLE

Observed and modeled patterns of covariability between low-level cloudiness and the structure of the trade-wind layer

Louise Nuijens[1,2], Brian Medeiros[3], Irina Sandu[4], and Maike Ahlgrimm[4]

[1]Atmosphere in the Earth System Department, Max Planck Institute for Meteorology, Hamburg, Germany, [2]Department of Earth, Atmospheric and Planetary Sciences, Massachusetts Institute of Technology, Cambridge, Massachusetts, USA, [3]Climate and Global Dynamics Division, National Center for Atmospheric Research, Boulder, Colorado, USA, [4]Physical Aspects Section, European Centre for Medium-Range Weather Forecasts, Shinfield Park, Reading, UK

Abstract We present patterns of covariability between low-level cloudiness and the trade-wind boundary layer structure using long-term measurements at a site representative of dynamical regimes with moderate subsidence or weak ascent. We compare these with ECMWF's Integrated Forecast System and 10 CMIP5 models. By using single-time step output at a single location, we find that models can produce a fairly realistic trade-wind layer structure in long-term means, but with unrealistic variability at shorter-time scales. The unrealistic variability in modeled cloudiness near the lifting condensation level (LCL) is due to stronger than observed relationships with mixed-layer relative humidity (RH) and temperature stratification at the mixed-layer top. Those relationships are weak in observations, or even of opposite sign, which can be explained by a negative feedback of convection on cloudiness. Cloudiness near cumulus tops at the trade-wind inversion instead varies more pronouncedly in observations on monthly time scales, whereby larger cloudiness relates to larger surface winds and stronger trade-wind inversions. However, these parameters appear to be a prerequisite, rather than strong controlling factors on cloudiness, because they do not explain submonthly variations in cloudiness. Models underestimate the strength of these relationships and diverge in particular in their responses to large-scale vertical motion. No model stands out by reproducing the observed behavior in all respects. These findings suggest that climate models do not realistically represent the physical processes that underlie the coupling between trade-wind clouds and their environments in present-day climate, which is relevant for how we interpret modeled cloud feedbacks.

1. Introduction

Steady winds and abundant fields of shallow trade-wind cumuli over the open ocean characterize the trades and give these regions in the subtropics an important role in climate. Surface evaporation under strong winds supplies the moisture that is needed for trade-wind cumuli to form. Trade-wind cumuli themselves transport moisture away from the surface throughout the lower troposphere, thereby setting its vertical structure and further increasing surface evaporation. By reflecting solar radiation trade-wind cumuli also increase the albedo, providing a modest (but persistent) cooling influence.

Although the trades are a relatively steady weather regime compared to other regions on Earth, the strength and direction of the trade-winds, sea surface temperatures, and large-scale vertical motion do show marked variability on daily, seasonal, and interannual time scales [*Brueck et al.*, 2015]. There is no doubt that changes in any of these parameters can induce changes in trade-wind clouds and the structure of the lower atmosphere, but their combined effects and resulting patterns of covariability are not sufficiently understood. Our objective is to expose relationships between trade-wind cloudiness and the structure of the trade-wind layer in observations and to provide insight into the overall sensitivity of trade-wind cloudiness to changes in the large-scale flow. Furthermore, we evaluate whether patterns of covariability between cloudiness and the trade-wind layer structure in global models are consistent with those observed.

In previous work, we showed that the amount of variance in trade-wind cloudiness in global (climate) models diverges from observations. Specifically, a common bias of climate models is to vary the amount of cloud near the lifting condensation level (LCL) more than is observed [*Nuijens et al.*, 2015]. Several models also

produce a trade-wind boundary layer that is too shallow, which leads to an underestimation of the variance in cloud amount in the cloud layer and near the trade-wind inversion. This study follows up on our previous work by relating the variability in cloudiness to variability in the structure of humidity, temperature, winds, and large-scale vertical motion. We will expose the ways in which models produce clouds, which may differ from nature, thereby providing insight into whether models capture the physical processes that underlie the coupling between clouds and their environment.

If global models can reproduce patterns of covariability in our current climate, we may have more confidence in their responses to future forcing scenarios, even though present-day variability is not necessarily a good proxy for future climate change. Climate models currently have different responses to future forcing scenarios due, in part, to different changes in trade-wind cloudiness. In some models trade-wind cloudiness decreases as climate warms, which amplifies the warming and leads to a high climate sensitivity. In other models trade-wind cloudiness increases, which leads to a low climate sensitivity [*Bony and Dufresne*, 2005; *Medeiros and Stevens*, 2011; *Vial et al.*, 2013]. *Brient et al.* [2015] show that the profile of cloud fraction in the trades in present-day climate is a good predictor for whether a climate model has a high or a low climate sensitivity. A high climate sensitivity model tends to have large values of cloudiness only near the LCL, much like stratocumulus, whereas a low-climate sensitivity model distributes cloudiness more evenly across a deeper trade-wind layer. *Sherwood et al.* [2014] further propose a link between the different responses of models and the different ways models mix moisture across the lower troposphere. For instance, they suggest that when a model efficiently transports moisture away from the surface it tends to have a high climate sensitivity. Such a model could efficiently dry the lower atmosphere as climate warms, which would lead to a reduction of low-level cloudiness.

Observations are crucial for evaluating whether changes in cloudiness with vertical moisture mixing in climate models are realistic, but over the open ocean measurements are mostly limited to space-borne remote sensing. However, observing the humidity and temperature structure in the lower atmosphere is challenging from space, especially in cloudy conditions. Space-borne instruments often lack the resolution to reveal vertical gradients that might be crucial for cloudiness. Shallow cumuli also have dimensions typically much smaller than satellite footprints. Furthermore, polar orbiting satellites view the same location on Earth only every couple of days, so that variability can only be studied on time scales of a month and longer. For climate models, a similar (practical) issue is true: conventional model output includes only monthly averages, which may hide variability on shorter-time scales that are critical to the mean behavior of clouds.

Ongoing approaches strategically address the need for evaluating global models against observations by making use of permanent ground-based meteorological sites that measure clouds and the structure of the atmosphere at a high temporal and vertical resolution. For instance, the Cloud-Associated Parameterizations Testbed (CAPT) applies weather forecast techniques to climate models to evaluate model parameterizations at measurement sites of the Atmospheric Radiation Measurement Program (ARM) of the U.S. Department of Energy [*Phillips et al.*, 2004]. Similarly, the KNMI Parameterization testbed (KPT) runs Large-Eddy Simulation (LES) and Single-Column Models (SCM) at ARM and European CloudNet sites [*Neggers et al.*, 2012]. Because these approaches sample and model clouds across a wide range of conditions, they have successfully led to the identification of systematic biases in modeled physics, such as a compensating error between cloud structure and radiative transfer due to cloud overlap assumptions [*Neggers and Siebesma*, 2013]. A few years ago, the Cloud Feedback Model Intercomparison Project (CFMIP) also initiated the so-called *cfSites* output, which includes single-time step output from many climate models at 120 strategically located sites [*Webb et al.*, 2015].

Unfortunately, the number of such sites is limited in the trades. To fill this gap in observational data, the Max-Planck Institute for Meteorology, jointly with the Caribbean Institute for Meteorology and Hydrology, installed a long-term measurement site in 2010: the Barbados Cloud Observatory (BCO, 13°N 59°W). The Island of Barbados is the most eastward located island in the West Indies facing the North Atlantic ocean. The airmasses and clouds advected to the site are therefore little influenced by land or the island itself (*Stevens et al.*, 2015). The location experiences moderate large-scale subsidence during boreal winter and weak ascent during boreal summer [*Brueck et al.*, 2015], which are exactly those regimes in which climate models differ the most in their structure of low-level clouds and response to warming. Under these large-scale conditions, the majority of trade-wind clouds found at Barbados are located well below 3 km,
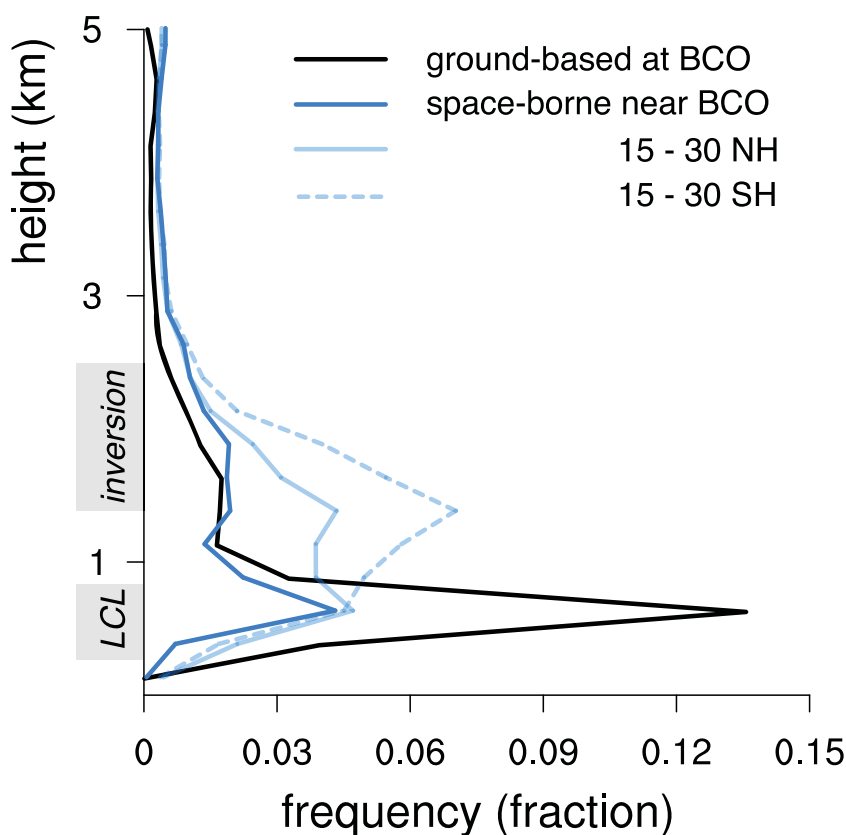
Figure 1. Lidar observations of the vertical distribution of cloud layer bases in the trades as viewed from ground (in black), respectively, from space (in blue). The distribution is made using 250 m bins and normalized by the total number of lidar profiles. It represents the frequency (fraction) of finding a cloud layer base at a given height. The distribution in black is derived from a laser ceilometer deployed at the BCO whose resolution corresponds to about 500 m. The distribution from the CALIOP lidar in blue is determined over a 5 × 10° area just upstream of Barbados at a 333 m footprint. We also show CALIOP distributions for the broader subtropics, including all oceans between 15 and 30° in the Northern and Southern Hemisphere. These distributions illustrate that the cloud profile below 5 km is marked by two important height levels where cloud layers tend to occur: near 700 m where cumuli have their base and near 1.5–2.5 km, where the inversion limits cumulus tops and stratiform layers can be found.

although deep convection and cirrus form an important contribution to high-level cloud cover and therefore to total cloud cover *Medeiros and Nuijens* [2015].

At Barbados, cloudy layers near the LCL at 700 m and near the trade-wind inversion at 1.5–2.5 km contribute most to low-level cloud cover [*Nuijens et al.*, 2014]. Cloud amount near the LCL is of interest because it is the dominant contribution to cloud cover and is relatively invariant in time. Moreover, cloud amount near the LCL at Barbados is remarkably similar to the cloud amount near the LCL over all subtropical oceans. This is illustrated in Figure 1, which is adapted from earlier papers [*Nuijens et al.*, 2014; *Medeiros et al.*, 2010]. The black line represents the distribution of cloud layer bases as viewed by a laser ceilometer with a footprint of ∼500 m deployed at the BCO between 2010 and 2014. The blue solid line represents the distribution of cloud layer bases as viewed by CALIOP (the lidar aboard the CALIPSO satellite), when it overpassed a region close to the BCO between 2010 and 2014. CALIOP has a comparable footprint of ∼333 m. The instruments give a sense of the height levels at which cloud layers are frequent and contribute to low-level cloud cover. Both instruments show that at Barbados cloud layers are most frequent near the LCL, although CALIOP underestimates the frequency. Likely this underestimation is caused by the attenuation of the lidar beam due to the longer path travelled and due to overlying high cloud. Notwithstanding, the frequency of CALIOP detecting a cloud layer near the LCL is remarkably similar for the BCO area and the subtropical oceans in the Northern Hemisphere and Southern Hemisphere, where the latter are shown by solid, respectively, dashed light blue profiles.

Cloud layers further aloft, near the trade-wind inversion, are of interest for another reason: the cloud amount at this level is much more variable in time and in space [*Nuijens et al.*, 2014]. At Barbados, the most

important contribution to cloud amount near the inversion is from stratiform layers near cumulus tops, followed by slanted tops of cumuli and short-lived patches of decaying cloud [*Nuijens et al.*, 2014]. The stratiform layers develop when trade-wind cumuli grow into a cloud layer that is capped by a relatively strong inversion [*Stevens et al.*, 2001; *Lock*, 2009], often typified as the intermediate or transition regime: between regions of stratocumulus underneath strong inversions at eastern ocean boundaries and regions of trade-wind cumuli in deeper boundary layers at western boundaries. Apparently this regime can be observed even this far west over the Atlantic. At the BCO, both the ceilometer at the BCO and CALIOP show a similar frequency of occurrence of cloud layers at the inversion. Over all NH and SH subtropical oceans, because larger areas of the intermediate and stratocumulus regimes are included, CALIOP detects a larger frequency of cloud near the inversion.

In the remainder of this manuscript, we will focus on these two height levels (the LCL and near the trade-wind inversion) to explain variability (or lack thereof) in cloudiness near the BCO. We perform similar exercises for the models, which include 10 climate models that have supplied the *cfSites* single-time step output for Barbados (or a nearby location), as well as the Integrated Forecast System (IFS) from the European Centre for Medium-Range Weather Forecasts (ECMWF), which has been run in a climate-model-like (year-long) integration mode. We will draw out similarities and differences from the observations, as well as how models diverge. Finally, we discuss how these results relate to climate change studies that hint at the importance of the shallowness of the cloud layer and vertical moisture mixing.

2. Data, Model Output and Methods

We use ground-based radar, lidar, and ceilometer data from the BCO combined with the ERA-Interim reanalysis product to derive relationships between cloudiness and the thermodynamic and kinetic structure of the trade-wind layer. We do the same for model output, which includes single-time step output from long integrations with the Integrated Forecast System (IFS) from the European Centre for Medium-Range Weather Forecasts (ECMWF) model and single-time step output from nine CMIP5 models. The following sections 2.1–2.4 describe the data and model output in more detail. We explain how we compare cloudiness in the models with that in the observations in section 2.5.

2.1. Barbados Cloud Observatory Data

The BCO is located on an eastward promontory of the island of Barbados (13.15°N, 59.4°W) and has a suite of instrumentation similar to the Department of Energy (DOE) ARM sites. The period April 2010 to April 2012 is used to derive statistics. Cloud cover (CC) is defined as the fraction of time (here either daily or monthly) that a ceilometer with a temporal resolution of 30 s measures a cloud base height overhead. We distinguish between the contribution of cloud at heights near the LCL to cloud cover (hereafter referred to as CC_{LCL}) and the contribution of cloud at heights further aloft (CC_{ALOFT}) by separating cloud bases that are detected below or above 1 km. Because the ceilometer measured almost continuously, these data provide some of our most important statistics.

When rainfall is strong enough, the ceilometer cannot detect a cloud base height. This is true for 60% of the rain events, which cover 7% of the data [*Nuijens et al.*, 2014]. Hence, for 4.2% of the observed profiles we cannot meaningfully separate the two components of CC_{LCL} and CC_{ALOFT}. For these 4.2%, we also cannot assess whether hydrometeors measured by the radar represent rain that falls through a detectable cloud base or rain that falls through the cloud layer out of slanted clouds. In our derivation of CC (as well as of cloud fraction (CF), see next paragraph) we exclude these 4.2% of data. This means that we underestimate total cloudiness in the observations by excluding heavily raining cloud, a bias we are willing to accept given our focus on qualitative behavior. Because these cases comprise only 4.2% of the record, they also do not substantially bias our results.

Cloud fraction (CF) profiles are derived from the Ka band (36 GHz) Doppler radar (KATRIN) when in a vertically pointing mode from January 2011 to mid-May 2011, October 2011 and from January 2012 to March 2012. Data include profiles every 10 s with a resolution of 30 m from 300 m up to 15 km. Radar returns with an equivalent radar reflectivity Z_e larger than -40 dBZ are defined as true hydrometeor returns. We exclude profiles for which no ceilometer cloud base height is available (strong rainfall, see above) and mask all returns below the lowest detected cloud base height that are likely drizzle.

Humidity and temperature profiles are measured with a multichannel Raman lidar, from 1 April 2011 to 1 April 2012. By measuring backscattered energy at the shifted Raman frequency, in the UV spectral range at 355 nm, the concentration of water vapor is derived. The pure rotational Raman spectra (PRRS) technique is used to derive air temperature [*Serikov and Bobrovnikov*, 2010]. The profiles of humidity and temperature are only available during nighttime when there is no interference of background solar light, between 0 and 8 UTC (20 —04 h local time). The lidar hatch also closes when the MRR detects rain-rates >0.05 mm h^{-1} at any height below 3 km. The raw data are averaged into 2 min profiles for water vapor and 1 hourly profiles for temperature, available at a 60 m resolution up to 15 km.

For more details on the sensitivity of CC and CF to our subjective thresholds of defining cloud, we refer the reader to *Nuijens et al.* [2014].

2.2. ERA-Interim
The ERA-Interim reanalysis product is used for daily and monthly profiles of the zonal and meridional wind components (u, v), and the vertical velocity (ω). It is based on the Cy31r2 version of the IFS [*Simmons et al.*, 2007]. The horizontal resolution (N128) of the quasiregular Gaussian grid is approximately 0.7° at 10°N. The vertical resolution is 61 model levels, with a pressure difference that increases from 4 hPa in the lowest levels to 40 hPa at a pressure of 440 hPa. The profiles are averaged over a 5° x 5° region upstream of Barbados.

2.3. ECMWF IFS
Long climate-model-like integrations are produced with the ECMWF IFS (ECMWF-LI). Unlike short integrations, which start every day from a state that is corrected by data assimilation procedures, these climate-model-like integrations are forecasts initialized only once a year, on the 1 August. They are performed at a T255 spectral resolution which corresponds roughly to a grid box of (75 $\times$ 75) km^2 at the Equator. The output is therefore comparable to the CMIP5 model output. We performed four of these long integrations for the years 2009–2012 with an IFS version that was operational between June 2013 and November 2013 (IFS Cycle 38r2). Single-time step (30 min) output was extracted from all these runs for a single grid point near Barbados, centered at 13.68°N, 59.06°W. The integrations are performed on 91 vertical levels, of which only the output for the lowest 31 levels is used, reaching from 10 to 7600 m with a spacing of 20 m at level 1 and 500 m at level 31. We found that qualitatively, the cloud fields in these long integrations are similar, or even closer to observations, than output from short (24 h) integrations [*Nuijens et al.*, 2015].

2.4. cfSites Output From CMIP5 Models
Single-time step output of nine climate models for a single grid point near Barbados is available through the cfSites initiative from the Cloud Feedback Model Intercomparison Project (CFMIP) [*Webb et al.*, 2015]. The output is produced from Atmospheric Model Intercomparison Project (AMIP) runs from 1976 to 2006, constrained by observed sea surface temperatures and sea ice. Although 30 years of data are available, 5 years (2001–2006) suffices for most of our analysis. The CMIP5 models and their acronyms are listed in Table 1. For all models, the location closest to Barbados at which cfSites output is produced is the BOMEX location (15°N 56.5°W). For the MPIM-E62 and MPIM-E63 models, we also produced output at a grid point near the BCO (13.2°N 59.4°W). Although the BOMEX location experiences fewer periods with mean rising motion, we believe it largely suffices for exploring models' behavior of trade-wind cloudiness. For most models, these grid points correspond to an area of about (100 $\times$ 100) km^2.

The MPIM-E62 and MPIM-E63 output is not obtained from the CMIP5 archive, but we have rerun the model with the newer ECHAM versions 6.2 and 6.3, wherein errors in the way statistics are accumulated have been fixed. For most models, single-time step output means 30 min output, except for the BCC model, which comes every 20 min. Two out of three time steps of the BCC model have zero cloud fractions everywhere, which seem an issue with the way the output has been produced. Therefore we only use every third time step. We do the same for the NCAR-C4 model, which has zero cloud fractions every other time step.

2.5. Cloud Fraction and Cloud Cover in Observations and Models
Cloudiness in models and in observations is inherently different. An often used technique to overcome these differences and compare models with observations is to use forward operators or cloud simulators implemented in models. These simulate how cloud predicted by the model would be measured by a given instrument. However, our analysis focuses on qualitative rather than quantitative behavior of cloudiness.

Table 1. List of Models Used in the Analysis, Including the Number of Model Levels up to 600 hPa (L_{600hPa}), and Between 950 and 900 hPa (L_{900hPa}), and References to Their Cloud and Convection Schemes[a]

No	Abbreviation	Model	Modeling Center	$L_{600hPa/900hPa}$	Cloud/Convection Scheme
1	ECWMF-LI	IFS long integration	European Centre for Medium Range Weather Forecasts	24/3	*Tiedtke* [1993]/ *Tiedtke* [1989]
2	MPIM-E63	MPI-ESM-LR ECHAM 6.3	Max-Planck Institute for Meteorology	11/2	*Tiedtke* [1989]/ *Sundqvist et al.* [1989]
3	MPIM-E62	MPI-ESM-LR ECHAM 6.2	Max-Planck Institute for Meteorology	11/2	*Tiedtke* [1989]/ *Sundqvist et al.* [1989]
4	BCC	BCC-CSM1.1	Beijing Climate Center	7/1	*Wu et al.* [2010]/ *Slingo* [1987]
5	CCCma	CanESM2	Canadian Centre for Climate Modelling and Analysis	14/2	*von Salzen et al.* [2005]/ /*McFarlane et al.* [2005]
6	IPSL	IPSL-CM5A-LR	Institut Pierre-Simon Laplace	11/1	*Bony and Emanuel* [2001]/ *Emanuel* [1993]
7	CNRM	CNRM-CM5	Centre National de Recherches Meteorologiques	11/2	*Gregory and Rowntree* [1990]/ *Ricard and Royer* [1993]
8	MOHC	HadGEM2-A	Met Office Hadley Centre	14/2	*Gregory and Rowntree* [1990]/ *Lock* [2009]
9	MRI	MRI-CGSM3	Meteorological Research Institute	12/1	*Yukimoto et al.* [2012]/ *Tiedtke* [1993]
10	NCAR-C4	CAM4	National Center of Atmospheric Research	7/1	*Rasch and Kristjansson* [1998]/ *Zhang and McFarlane* [1995]
11	NCAR-C5	CAM5	National Center of Atmospheric Research	11/2	*Gettelman et al.* [2010]/ *Zhang and McFarlane* [1995]

[a]All models use the BOMEX location, except the ECMWF-LI, MPIM-E63, and MPIM-E62, which use a grid point just upstream of Barbados. All models have output every 30 min. For the BCC and NCAR-C4 model, only every second output step is used in the analysis, see section 2.4.

For instance, we study the shape of the cloud fraction profile or the variability of cloud fraction in time. To identify differences in such qualitative aspects between models and observations, it is not necessary to apply a forward operating technique. For a similar reason, we also do not interpolate the observations onto a coarser vertical grid that is representative of the models' grids.

We do account for the difference in temporal or horizontal resolution: the observations have a footprint of just a few tens of meters, whereas a single model grid point is equivalent to an area of about (100×100) km^2. The BCO time series is first averaged to a period that represents the time needed for an air mass to travel across a 100 km distance. Wind speeds are observed to be about 7 ms^{-1} on average, which equals 4 h of BCO measurements. In all figures and analysis where time scales are mentioned the averaging of the BCO data is implicit, unless we explicitly state otherwise.

CF refers to the amount of cloud that is present at a given height or pressure level, whereas CC is the total amount of cloud projected onto the surface, only from cloud that is present at heights below 5 km ($\approx$550 hPa). As discussed in the introduction, we focus on cloudiness at two levels: near the LCL and near the tops of the deepest cumuli, just below the trade-wind inversion [see also *Nuijens et al.*, 2014 and the continuing discussion on in section 3]. We define CF_{LCL} in observations and in models as the cloud amount at the LCL, which we take as the level at which the RH profile maximizes. A list of LCL's for the observations and models is given in Table 2. Furthermore, we define CF_{ALOFT} as the average cloud fraction between 850 and 800 hPa.

In the observations, CF is intermittent due to frequent downtimes of the cloud radar (section 2.1). For certain analyses, we therefore use the more continuous

Table 2. The Approximate Level of Cloud Base or the LCL, Taken as the Level at Which the Mean RH Profile Maximizes, Restricted to Levels With $p > 850$ hPa. Also Tabulated is the Ratio of the Variance in CF_{ALOFT} to CF_{LCL} (for the Models) and of the Variance in CC_{ALOFT} to CC_{LCL} (for the Observations)

Abbreviation	LCL	$\sigma^2 CF_{ALOFT}/\sigma^2 CF_{LCL}$
BCO	925	1.8
ECMWF-LI	967	1.0
MPIM-E63	941	0.2
MPIM-E62	941	0.0
BCC	945	1.3
CCCma	911	0.03
IPSL	978	0.2
CNRM	904	0.5
MOHC	930	0.8
MRI	929	2.1
NCAR-C4	930	1.0
NCAR-C5	936	0.5

time series of CC instead, which we separate into two contributions: from cloud bases detected below 1 km (CC_{LCL}) and above 1 km (CC_{ALOFT}), which qualitatively capture variations in CF_{LCL} and CF_{ALOFT} [*Nuijens et al.*, 2014]. Because we contrast environments in which cloudiness is abundant or not, focusing on cloudiness more qualitatively than quantitatively, we freely use observed CC_{LCL} or CC_{ALOFT} alongside modeled CF_{LCL} and CF_{ALOFT}. Because many models just have one or two vertical levels between 950 and 900 hPa, corresponding to the mean LCL and 1 km, their CC_{LCL} would principally be equal or very close to CF_{LCL}. When we use observed CC instead of observed CF, we indicate this in the figure caption. For simplicity we just refer to CF throughout the text, but flagged with a star (CF^*_{LCL}, CF^*_{ALOFT}).

3. Vertical Structure of Clouds and Their Environment

This section provides a general overview of the most important features of the trade-wind layer including the cloud profile. First, we describe the observed and modeled long-term mean profiles for periods of moderate subsidence and of weak ascent. Second, we discuss the variability in cloudiness and the structure of the trade-wind layer on shorter daily time scales.

3.1. Long-Term Means

In the dry season from December through May, Barbados experiences large-scale flow that is typical of the fair-weather trade-wind regime. The region is in the subsiding branch of the Hadley circulation and strong winds with a northerly component advect relatively colder and drier air from higher latitudes toward Barbados. As the InterTropical Convergence Zone (ITCZ) migrates northward in the wet season from June to November, the region experiences moderate rising motion instead ($\omega < 0$). Sea surface temperatures are about 2 K higher and smaller pressure gradients between the subtropics and Equator drive weaker winds [*Brueck et al.*, 2015]. Deep convective events and even an occasional hurricane are not uncommon.

Despite these differences in large-scale flow and free tropospheric temperature and humidity, the dry and the wet season have similar cloud structures. Mean profiles of cloud fraction (CF), the relative humidity (RH), virtual potential temperature (θ_v), and the frequency distribution of inversion levels (p_{inv}) are shown in Figure 2. The black line corresponds to January to March (the dry season) and the grey line to September to November (the wet season). The lower atmosphere is both drier and colder during the dry season. Cloud base height (LCL) is located near 925 hPa, which coincides with a maximum in RH. The layer near the LCL at the top of the well-mixed layer is often called the transition layer, because RH more sharply decreases than in the (upper) cloud layer. In the dry season, the LCL is somewhat higher, the transition layer is more pronounced and a separation between the cloud layer and the inversion layer is distinct. However, even during the dry season, the location of the inversion (p_{inv}, which is the pressure level of the maximum θ_v gradient at $p > 600$ hPa) can range anywhere between 825 and 600 hPa on a daily basis. Such variability smooths the inversion structure when profiles are averaged; individual profiles are likely to have much more pronounced inversions than the mean.

In both seasons, CF throughout the cloud layer is about 0.08, but there are some important differences. The wet season gets more deep convection, which increases CF and RH above 800 hPa, but reduces CF near 825 hPa due to less stratiform cloud layers near cumulus tops [*Nuijens et al.*, 2014]. Also note that there is a hint of more frequent stable layers near 950 hPa from the distribution of p_{inv} in Figure 2, which could be a result from compensating downward motion from deep convection, which stabilizes the environment, or from evaporation of rain below cloud base.

The smaller CF near 825 hPa in the wet season is responsible for a modest reduction in low-level cloud cover (CC) [*Nuijens et al.*, 2014]. This modest seasonality in CC is not just apparent in the BCO measurements, but also in data from active and passive satellite sensors for a region upstream of Barbados [*Medeiros and Nuijens*, 2015; *Brueck et al.*, 2015].

Most models have a maximum in CF near the top of the well-mixed layer with values less than 0.3 (Figure 2, remaining plots). They thus capture the basic feature of trade-wind cloudiness: a partially cloudy layer with clouds that are produced most frequently near the LCL. Many models place the trade-wind inversion near and above 825 hPa and therefore produce cloud layer depths similar to observations. Moreover, several models reproduce the layered structure of the trade-wind layer, including the increase in RH in the well-
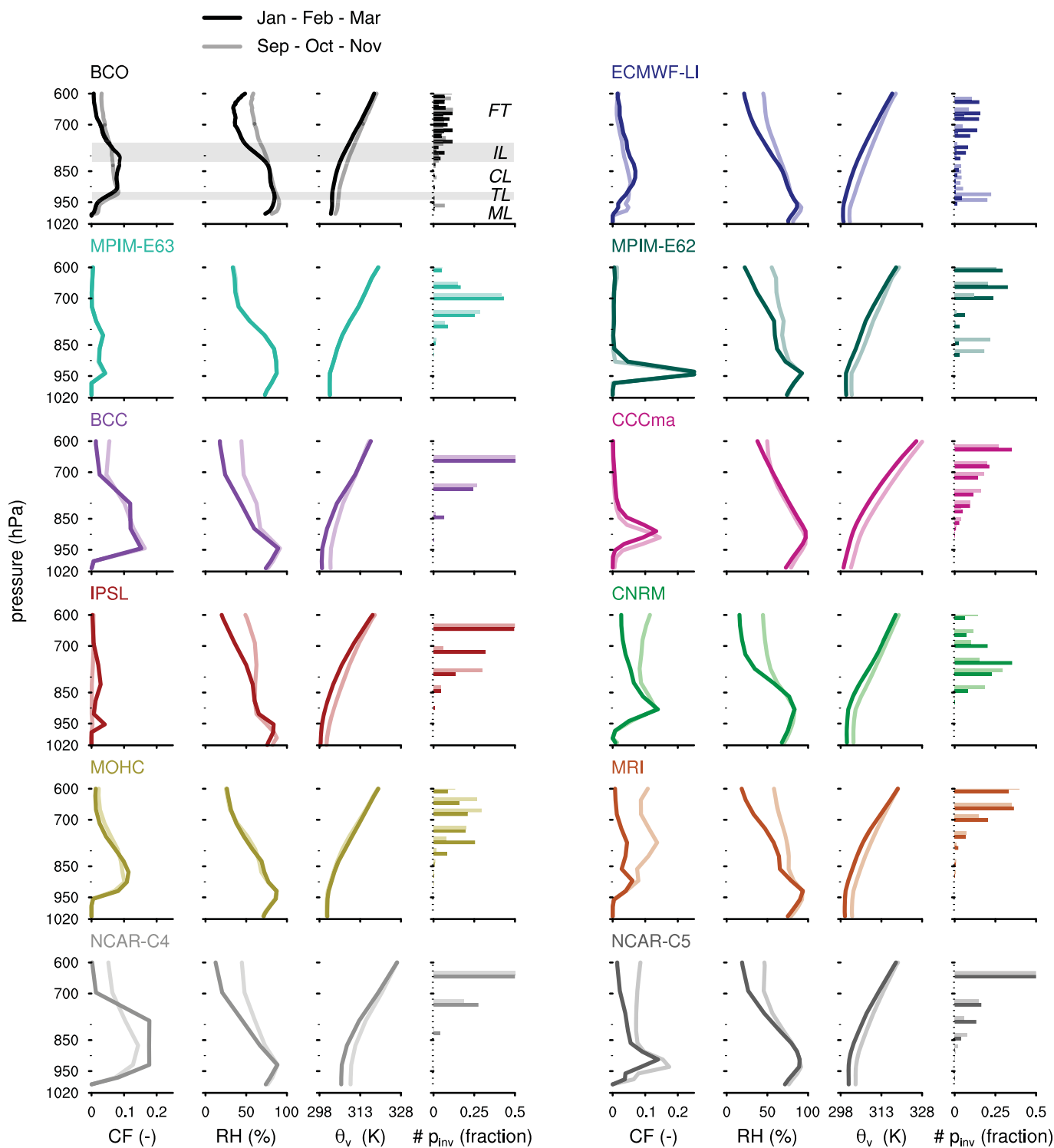
Figure 2. Mean cloud and thermodynamic profiles are plotted, representative for the period January–March (dry season) and September–November (wet season), from Barbados Cloud Observatory (BCO) data and from model output for a location nearby Barbados (EMCWF-LI, MPIM-E63, MPIM-E62) or the BOMEX location (all other models). January–March is depicted by solid lines, whereas September–November is depicted by lighter-toned transparent lines. Variables shown from left to right: cloud fraction (CF), the relative humidity (RH), the virtual potential temperature θ_v, and the frequency (fraction) of finding inversion layers at a given pressure level: p_{inv}. Abbreviations for the five layers that are identified in the BCO profiles refer to: ML = well-mixed layer, TL = transition layer, CL = cloud (cumulus) layer, IL = inversion layer, and FT = free troposphere.

mixed layer up to the LCL and a decrease in RH in the cloud layer. Some models even show a hint of a transition layer in their RH profiles and distribution of p_{inv}.

Many models are systematically too dry in the upper part of the cloud layer (850–825 hPa), but most of them predict the warming and moistening toward the wet season. The associated changes in the CF profile at levels below 850 hPa are small, consistent with the observations. Models thus reproduce the robustness of the trade-wind layer. Nevertheless, no model stands out as performing particularly well at capturing the finer details, including the difference in LCL between the seasons, the invariance of CF near the LCL and most importantly, the decrease in CF near 825 hPa.

These points will be discussed in more detail when we relate cloudiness to the structure of the trade-wind layer (section 4.2). First, we will take a closer look at how models vary the structure of cloud and humidity on shorter-time scales.

3.2. Short-Term Variability
How a model arrives at its mean CF profile can be very different from the observations. In the observations, individual days experience clouds that are fairly evenly distributed over a layer from the LCL to the mean inversion height, whereas in the models the vertical distribution of clouds can differ substantially from one day to the next.

The shape of the CF profile can be measured by a parameter $\gamma = CF_{LCL}/(CF_{LCL} + CF_{ALOFT})$, which represents how bottom-heavy (large γ) or top-heavy (small γ) the CF profile is *Brient et al.* [2015]. Distributions of γ from daily CF profiles are shown in black in Figures 3a (dry season) and 3d (wet season). Values for γ are always less than 0.6, which implies that CF is distributed across the cloud layer and tends to be emphasized near the top of the cloud layer especially in the dry season.

Compared to observations, models differ greatly in their distributions of γ. Several models shift between very bottom-heavy ($\gamma > 0.9$) and top-heavy profiles ($\gamma < 0.1$). This behavior of γ is related to frequent occurrences of $CF_{LCL} = 0$ or $CF_{ALOFT} = 0$ (square markers on the left outset of Figures 3b, 3c, 3e, and 3f). However, in the observations, there are very few days on which CF at either level is completely absent. This is even more true for CC_{LCL} (in black solid lines) because it represents a cloud amount integrated over many observed heights within one model layer.

In observations, the total variance in CF_{ALOFT} is about twice that of CF_{LCL} (see Table 2, whose values were previously shown in *Nuijens et al.* [2015]). Hence, variability in cloudiness near the inversion is the dominant contributor to variability in low-level CC. In contrast, six out of nine models have in total more variance in CF_{LCL} than in CF_{ALOFT} (Table 2), which is caused by their frequent dissipation of CF near the LCL.

Periods with zero CF_{LCL} can in some models last for days or weeks at a time [*Nuijens et al.*, 2015], which suggests that the behavior is not random. In the following sections, we analyze if such behavior can be linked to the modeled trade-wind structure and large-scale flow.

4. Patterns of Covariability of Cloud and Environment

The results presented in previous sections hint that patterns of covariability between cloudiness and the environment are systematically different in the models compared to observations. For CF_{LCL} and CF_{ALOFT}, respectively, section 4.1 and 4.2 reveal the anomalous profiles of RH, absolute humidity q, potential temperature θ, vertical velocity ω, and the wind components u, v for months with large and small CF—in observations and models. The anomalies are taken with respect to a yearly running mean centered on each month.

Furthermore, we perform regressions between CF and parameters that one may call large-scale predictors, which have been found important for explaining variations in cloudiness in previous studies [*Brueck et al.*, 2015]. These parameters include the RH averaged over the well-mixed layer ($\langle RH \rangle_{ML}$), the vertical difference in RH between 850 hPa and the LCL ($\Delta_{CL} RH = RH_{850} - RH_{LCL}$) and the vertical difference in RH across the inversion layer ($\Delta_{IL} RH = RH_{700} - RH_{850}$). Furthermore, the potential temperature lapse rate across the transition layer or mixed-layer top is considered, $d\theta/dz_{TL}$, which for the observations is derived between 1000 and 900 hPa and for the models between one model level above and below the LCL (which are not always separated by 100 hPa, hence we take the actual gradient here instead). The free tropospheric θ lapse rate is
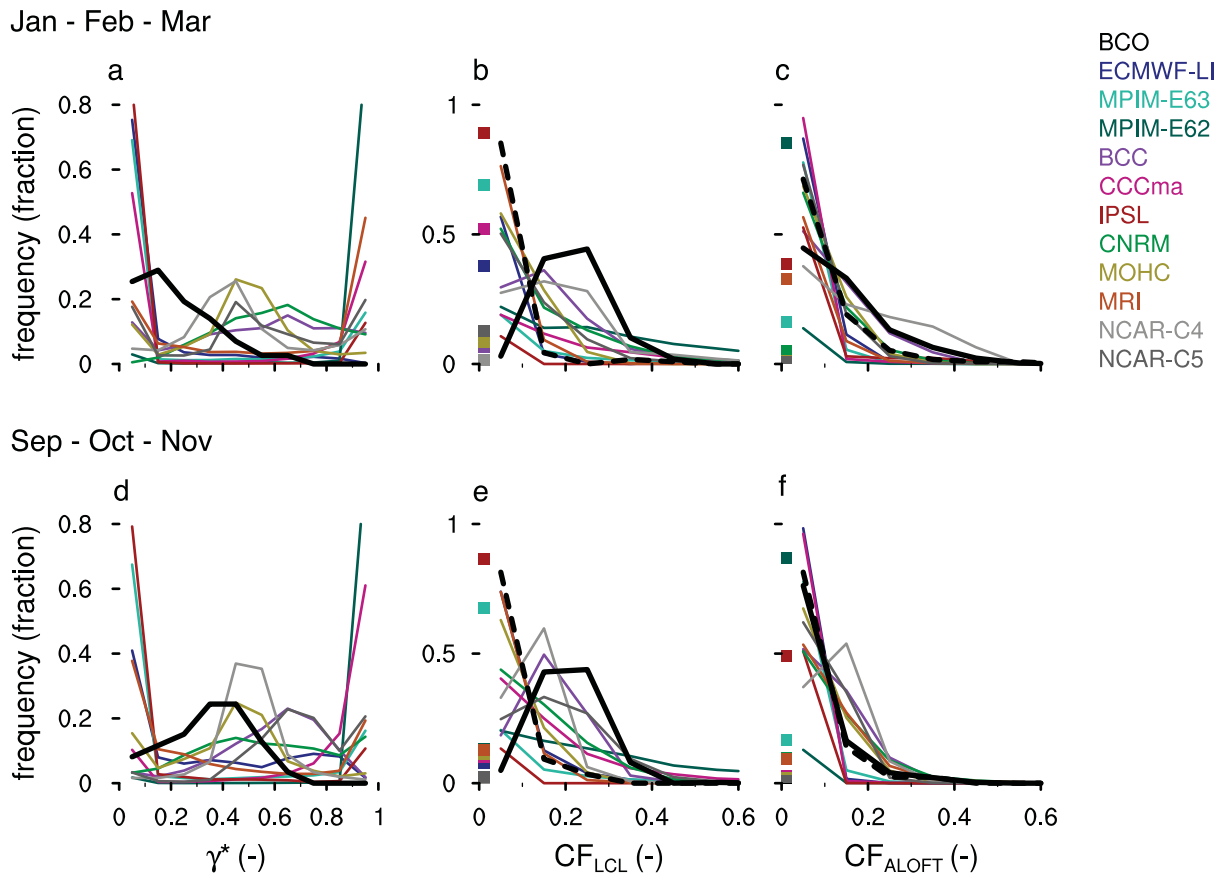
Figure 3. A parameter that measures the shape of the profile of CF and CF at selected levels are shown for the period January–March (top row) and September–November (bottom row). The three plots are frequency distributions of: (a,d) $\gamma*$, which represents how bottom-heavy (large γ) or top-heavy (small γ) the CF profile is, modified after *Brient et al.* [2015]; (b,e) CF_{LCL} (Table 2); and (c,f) CF_{ALOFT}. For definitions, see section 2.5 and 3.2. The observed CF_{LCL} and CF_{ALOFT} are shown in dashed black lines and the observed CC_{LCL} and CC_{ALOFT} are shown separately in solid black lines. All parameters are derived from daily mean profiles. The minor tick marks indicate the binning that is used. In Figures 3c, 3d, 3f, and 3g, the bin 0–0.1 excludes the frequency of finding CF = 0, these are shown separately by the square markers at the left outset of each plot.

also considered, whereby $\Delta_{IL}\theta$ is determined between 750 and 600 hPa. Last, the vertical velocity at 825 hPa (ω_{825}) and the near-surface wind speed U_{L0} are included.

4.1. Cloudiness Near the LCL
4.1.1. Observed Versus Modeled Seasonal Patterns

In observations, the differences in $CF*_{LCL}$ from one month to the next are generally modest, but there are a few notable differences. Months with larger $CF*_{LCL}$ (thick black lines, Figure 4) have a drier well-mixed layer, a relatively moist cumulus layer and a very dry and warm layer near and above the inversion between 825 and 600 hPa compared to months with smaller $CF*_{LCL}$ (thin black lines). The dry and warm air between 825 and 600 hPa is likely associated with the intrusion of Saharan Dry Air layers, which occurs throughout late spring and early summer [*Carlson and Prospero*, 1972].

Relatively cold cloud layers over warm well-mixed layers destabilize the cloud layer to convection and triggers abundant cloudiness within the first 1.5 km above the LCL. The cloudiest months also have stronger winds, with a more pronounced northerly component, which is consistent with the air masses being relatively cold (in θ) and dry (in q). A separation in the vertical wind component, ω, is only visible above 825 hPa, which suggests that months with large-scale subsidence generally have larger $CF*_{LCL}$, but that ω is not a decisive factor.

We have already seen that models tend to have more variance in CF_{LCL} than is observed, with frequent occurrences of $CF_{LCL} = 0$ (Table 2 and Figure 3c). Therefore it might not come as a surprise that models covary CF_{LCL} with the environment in a number of ways. As the anomaly profiles for a subset of models illustrate, increases in humidity and temperature, winds, and subsidence can either increase or decrease
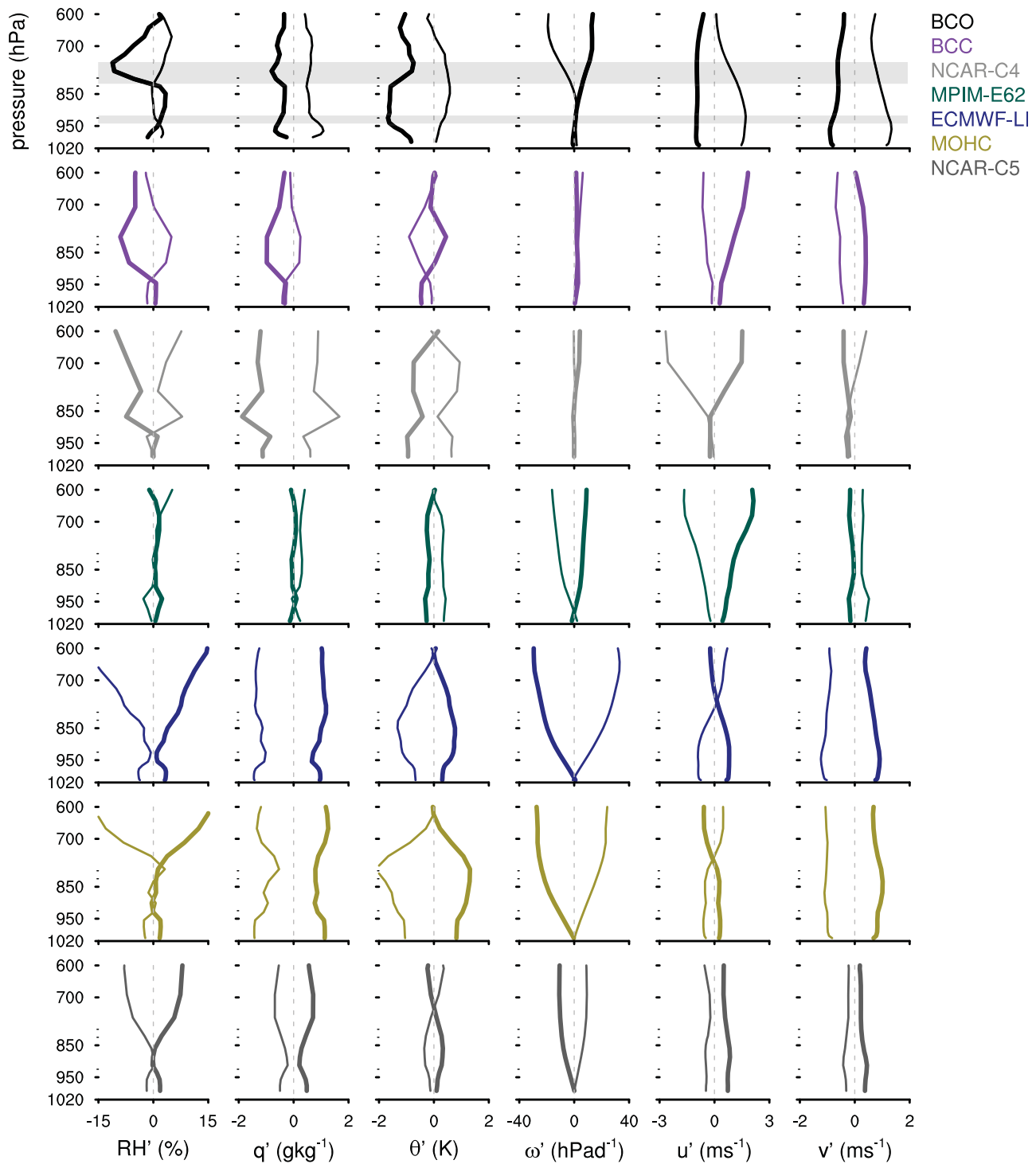
Figure 4. The anomalies in thermodynamic and kinetic profiles for months with large values of CF_{LCL} (thick lines) and small values of CF_{LCL} (thin lines). The anomalies are taken with respect to a yearly running mean centered on each month. (top row) The BCO data are shown, whereby the lines correspond to the lower and upper quartile of ordered anomalies in CC_{LCL} instead of CF_{LCL}. The following rows show the same, but for the models using CF_{LCL}. We show only those models in which the variance in monthly CF_{LCL} is better explained by parameters that represent the large-scale state than in observations (Table 3).

CF_{LCL} (Figure 4). Some models are close to the observed behavior (BCC, NCAR-C4), but have weaker and more southerly winds at times of large cloudiness instead. Other models show very little separation in profiles (MPIM-E62) or produce more CF_{LCL} during months with mean rising motion ($\omega < 0$) that have a moister and warmer trade-wind layer (ECMWF-LI, MOHC, and NCAR-C5).

Table 3. From Left to Right: the Total Fraction of Variance in Daily CF_{LCL} (Models) and CC_{LCL} (Observations) Explained Using Six Parameters (see below); the Parameter X_s That Best Explains Variance in Daily CF_{LCL} Using a Single Regression; r^2, the Fraction of Variance Explained by X_s; the Parameter X_m That Best Explains Variance in Daily CF_{LCL} Using a Multivariate Regression (in Which Other Parameters are Held Constant)[a]. The Following Four Columns Show the Same Information for Monthly CF_{LCL}

Abbreviation	R^2 (1d)	X_s (1d)	r^2 (1d)	X_m (1d)	R^2 (30d)	X_s (30d)	r^2 (30d)	X_m (30d)
BCO	0.24	ω_{825}	0.10	$\langle RH \rangle_{ML}$	0.56	$d\theta/dz_{TL}$	0.30	U_{L0}
ECMWF-LI	0.28	$\langle RH \rangle_{ML}$	0.21	$\langle RH \rangle_{ML}$	0.72	ω_{825}	0.62	$\langle RH \rangle_{ML}$
MPIM-E63	0.28	$\langle RH \rangle_{ML}$	0.25	$\langle RH \rangle_{ML}$	0.62	$\langle RH \rangle_{ML}$	0.50	$\langle RH \rangle_{ML}$
MPIM-E62	0.66	$\langle RH \rangle_{ML}$	0.61	$\langle RH \rangle_{ML}$	0.80	$\langle RH \rangle_{ML}$	0.61	$\langle RH \rangle_{ML}$
BCC	0.56	$\langle RH \rangle_{ML}$	0.42	$\langle RH \rangle_{ML}$	0.72	$d\theta/dz_{TL}$	0.63	$d\theta/dz_{TL}$
CCCma	0.27	$\langle RH \rangle_{ML}$	0.13	$\langle RH \rangle_{ML}$	0.52	$\langle RH \rangle_{ML}$	0.31	$\langle RH \rangle_{ML}$
IPSL	0.02				0.12			
CNRM	0.44	$d\theta/dz_{TL}$	0.28	$d\theta/dz_{TL}$	0.67	$d\theta/dz_{TL}$	0.23	$d\theta/dz_{TL}$
MOHC	0.48	ω_{825}	0.38	$d\theta/dz_{TL}$	0.83	$d\theta/dz_{TL}$	0.69	$d\theta/dz_{TL}$
MRI	0.30	Δ_{CL} RH	0.15	$d\theta/dz_{TL}$	0.49	Δ_{CL} RH	0.10	$\langle RH \rangle_{ML}$
NCAR-C4	0.66	$d\theta/dz_{TL}$	0.53	$d\theta/dz_{TL}$	0.75	$d\theta/dz_{TL}$	0.53	$d\theta/dz_{TL}$
NCAR-C5	0.50	$\langle RH \rangle_{ML}$	0.46	$\langle RH \rangle_{ML}$	0.67	$\langle RH \rangle_{ML}$	0.58	$d\theta/dz_{TL}$

[a]The parameters used are: (1) the average RH in the well-mixed layer $\langle RH \rangle_{ML}$, (2) the difference in RH across the cloud layer Δ_{CL} RH, (3) the difference in RH across the inversion layer Δ_{IL} RH, (4) the θ lapse rate across the transition layer or mixed-layer top $d\theta/dz_{TL}$, (5) the vertical velocity at 825hPa ω_{825}, and (6) the near surface wind speed U_{L0}.

In the following section, we discuss the relationships of cloudiness with the environment in more detail by looking at daily and monthly time scales. To simplify the discussion, we perform single and multi-variate regressions of cloudiness with the large-scale predictors defined above.

4.1.2. Predictors of Cloudiness

To facilitate the comparison between models and observations, which differ in their magnitudes and in their variances of CF, a standardized regression is used whereby the regression coefficients are scaled by the ratio of the standard deviation of a parameter to the standard deviation of CF. Table 3 lists the parameter that explains most of the variance, using a single regression for each parameter, as well as using a multivariate regression, which basically removes the effect of covarying parameters that may strengthen or weaken individual relationships. The single regression coefficients are also plotted in Figure 5 for the different time scales. The regressions for different time scales are created by first removing the long-term mean
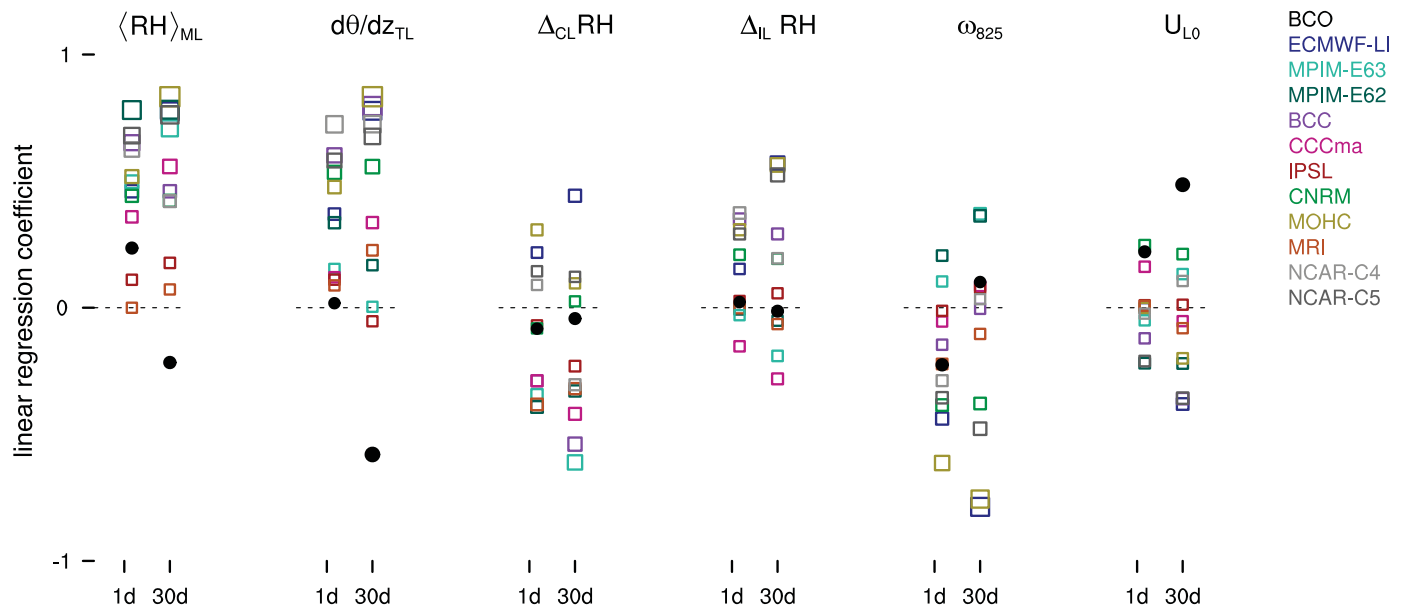

Figure 5. The linear regression coefficient between CF_{LCL} (models) or CC_{LCL} (observations) with different parameters X_s determined on different time scales. The parameters include $\langle RH \rangle_{ML}$, $\Delta_{CL}RH$, Δ_{IL} RH, $d\theta/dz_{TL}$, ω_{825} and U_{L0}, which are introduced in the text (section 4.1.2) and the caption of Table 3. The time scales range from daily anomalies (from monthly means) to monthly anomalies (from yearly means). The observations are denoted by black circles. Models are denoted by squared markers, whose size is scaled by the amount of variance explained.

before performing the regression. For instance, monthly means are subtracted from daily means and yearly means are subtracted from monthly means.

The observed regressions for CF_{*LCL} turn out to be overall small and negligible for most parameters—including RH. Altogether the selected set of parameters explains 24% of the observed total variance on daily time scales and 56% of the observed total variance on monthly time scales. U_{L0} and $d\theta/dz_{TL}$ are the parameters that best explain monthly variations in $CF*_{LCL}$ (30% each).

All models run counter to the observations by producing excessive CF_{LCL} when the well-mixed layer is relatively humid and topped by a more stable transition layer. $\langle RH \rangle_{ML}$ and $d\theta/dz_{TL}$ explain at least half of the variance in monthly CF_{LCL} (last column, Table 3). In addition, the models lack the observed relationships between CF_{LCL} and $U_{L0,}$ or that relationship has the opposite sign.

The time series in Figure 6 illustrate the relationship between CF_{LCL} and RH in observations (Figure 6, top two plots) and a few models for which the regression coefficients between CF_{LCL} and $\langle RH \rangle_{ML}$ are larger than 0.7 at monthly time scales. The observations show that CC_{LCL} has day-to-day variations, but stays close to 20% on longer-time scales. Although covariations between daily RH_{LCL} and CF_{LCL} can be observed, CF_{LCL} does not exhibit the multiday (i.e., synoptic) fluctuations that RH does. The models' single-time step behavior shows that their variances in CF_{LCL} are much larger than observed, which in some models (e.g., MPIM-E62) are tightly linked to RH variations (cf. Figure 5).

Behind the behavior, we derive from the models appears to linger well-established relationships between low-level cloudiness, relative humidity, the stability of the lower atmosphere, and the large-scale vertical velocity, which in climatologies separate patterns of cloudiness along latitude and inspired cloud parameterizations decades ago. For example, many climate models use a diagnostic cloud scheme whereby CF is some function of the RH, assuming that condensation on subgrid scales is related to a larger-scale synoptic regime that makes an imprint on the mean relative humidity [*Slingo*, 1980; *Sundqvist et al.*, 1989; *Qu et al.*, 2014]. Larger cloud amounts, such as belonging to stratocumulus decks, have also been linked to regions with enhanced lower tropospheric stability [*Klein and Hartmann*, 1993]. Therefore, vertical temperature gradients, as well as vertical velocity ω, have likely made their way into parameterizations of cloudiness. However, because these parameters do not reflect the dominant mechanisms that control CF on shorter-time scales, they might lead to overly strong dependencies.

In the following section, we explain why relationships between CF_{*LCL} and the large-scale environment are small on short-time scales in the observations. We hypothesize about the underlying processes that lead to the observed relationships with U_{L0} and $d\theta/dz_{TL}$ and discuss reasons for the somewhat counterintuitive result that $\langle RH \rangle_{ML}$ plays only a minor role.

4.1.3. Constraints on Cloudiness Near the LCL in Nature

In the observations, there is little evidence for strong controlling factors on CF_{*LCL}. One of the explanations for this is that CF_{*LCL}, when averaged over a day or longer has relatively little variance (compared to CF_{*ALOFT}, see also Table 2). *Nuijens et al.* [2015] show that 60% of the total variance in CF_{*LCL} is contained on time scales less than a day. This suggests that processes that have relatively short-time scales are important in regulating cloudiness, which in turn are relatively insensitive to changes in the large-scale flow, such as large-scale subsidence or large-scale relative humidity. For instance, larger CF_{*LCL} is found during months with lower $\langle RH \rangle_{ML}$ (Figure 5), which shows that RH is not a decisive factor.

Using the high-resolution nighttime humidity measurements at the BCO, which provide a humidity profile every 2 min, we find that the location of the mixed-layer top (η) with respect to the LCL of air parcels near the surface is decisive for cloudiness near the LCL on short-time scales. Humidity anomalies for 15 min periods during which CF_{*LCL} is large or small (compared to the nighttime mean) are most pronounced near 700 m, but less so toward the surface (Figure 7). Because the layer below η tends to be well-mixed, we expect q to be relatively constant with height, which implies that the signal in q at 700 m merely reflects an increase of η.

This finding is not surprising. Going back to early work by *Malkus* [1958], it has been recognized that for cumulus clouds to form, buoyant air parcels need to ascend through a stable layer, the transition layer, which is similar to a layer of convective inhibition in studies of deep convection. The transition layer is marked by a small decrease in absolute humidity and increase in temperature, which reflects the penetrative nature of the dry convection in the sub-cloud layer: the overshooting and downward mixing of
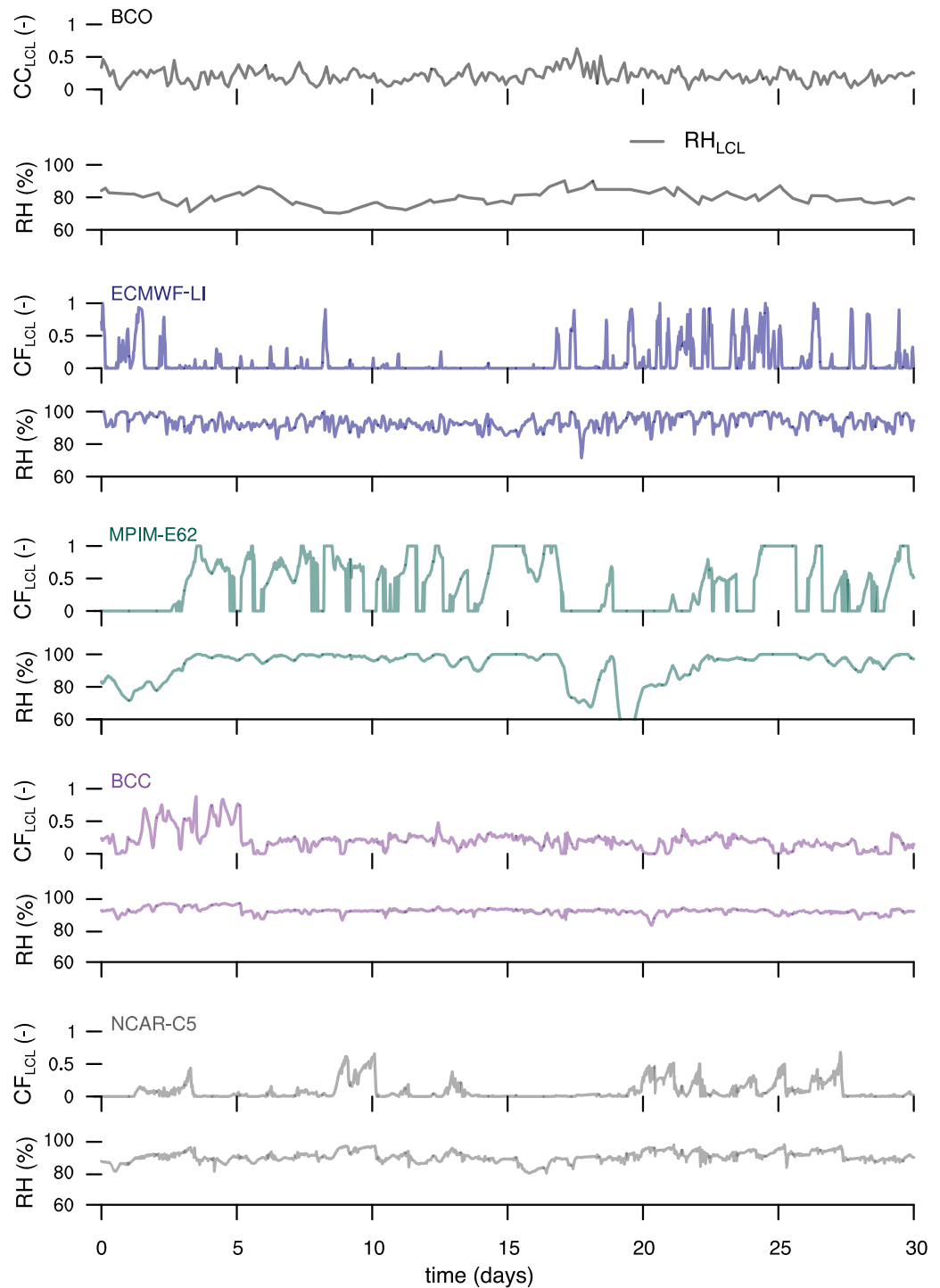
Figure 6. A sample time series of 4 hourly CC_{LCL} (observations) and CF_{LCL} (models), as well as RH near the LCL. Note that observed RH has a lower temporal resolution, because it is available during nighttime only. Daytime values are simply constructed by interpolating between nighttime values.

relatively dry and warm air. This is illustrated in part 1 of Figure 8, adapted from *Neggers et al.* [2006]. In this illustration, we also indicate that the LCL is not just one height level, but at a range of levels, because buoyant parcels ascend from different levels in the well-mixed layer that have different humidity and temperature values. An increase in η with respect to the mean LCL, or vice-versa, a decrease of the mean LCL, will increase the fraction of parcels that reach saturation.
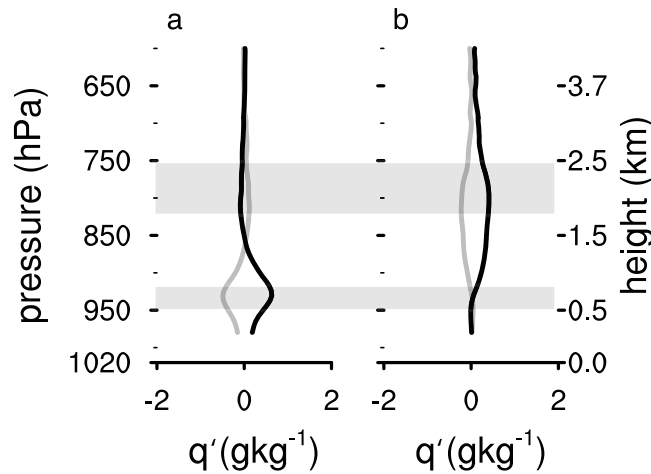
Figure 7. Observed anomalous profiles of specific humidity q for 15 min periods with large values of cloudiness, denoted in black, and small values of cloudiness, denoted in grey. Cloudiness is measured by CC_{LCL} (a) and CC_{ALOFT} (b). The anomalies are taken with respect to the 8 hourly nighttime mean q profile, of which the lower and upper quartiles are shown. Because the observed temperature profiles only have an hourly resolution, temperature and therefore relative humidity anomalies are not shown.

A handful of studies in the past decade have built simple models of cumulus convection around the idea that the location of η with respect to the LCL, as well as the difference in humidity and temperature across the mixed-layer top, are regulated by cumulus convection itself (sometimes called the cumulus-valve mechanism) [*Albrecht et al.*, 1979; *Neggers et al.*, 2006; *Stevens*, 2006; *Fletcher and Bretherton*, 2010]. These ideas are helpful to understand observed modulations of η on relatively short-time scales and provide an explanation for why $CF*_{LCL}$ has little variance on longer-time scales. In such models, the mass budget of the well-mixed layer is written as:

$$\frac{d\eta}{dt}=E-M+\bar{w}_\eta \qquad (1)$$

where E is the rate at which cloud layer air is entrained into the subcloud layer ($E>0$, and ≈ 1 cms^{-1}). $\bar{w}_\eta$ is the large-scale vertical velocity, which is <0 downward and ≈ 0.5 cms^{-1}. Finally, M is the mass removed from the layer by convection. M can be written as the product of w_c, the vertical velocity in the positively buoyant cores of clouds, and of a_c, the cloud core fraction:

$$M=w_c\,a_c \qquad (2)$$

A typical core fraction a_c is on the order of a few percent (0.01–0.05), which may be understood from the balance $a_c \approx \frac{E-\bar{w}_\eta}{w_c}$ and assuming equilibrium ($\frac{d\eta}{dt}=0$). For updrafts with $w_c \approx 1$ ms^{-1} this leads to $M \approx 1$ cms^{-1}. Let us imagine a scenario by which the well-mixed layer is perturbed and q increases by δq, which lowers the LCL and leads to a ten-fold increase in a_c (Figure 8, #1 and 2,). Following equation (2), M consequently increases by an order of magnitude to 10 cms^{-1}, which has the potential to lower η by a 100 m in only 1000 s. The net effect is to lower η, bringing it closer to the mean LCL again, which constitutes the negative feedback. At the same time, the amount of dry air that is pushed down by convective downdrafts helps
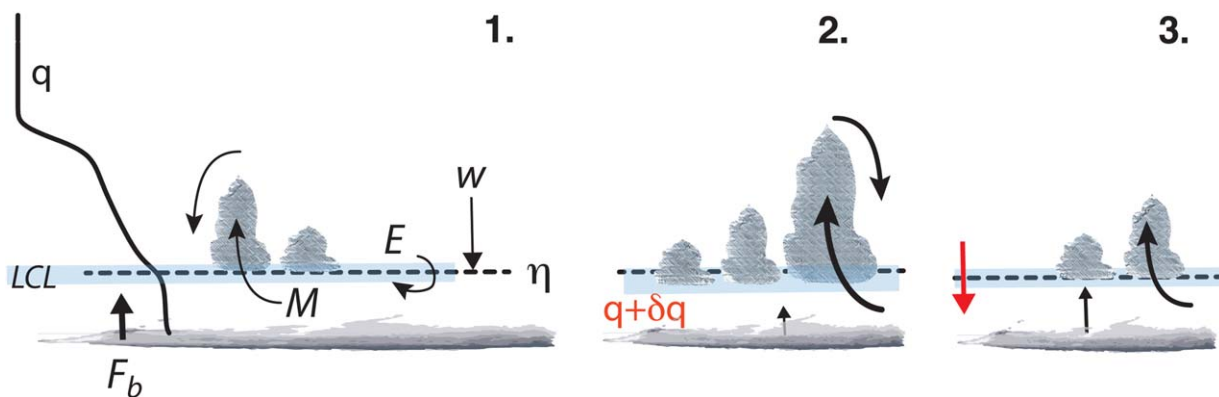

Figure 8. Illustration of the negative feedback mechanism that constrains cloud amount near cloud base, adapted from a Figure by *Neggers et al.* [2006]. In (1) a typical humidity profile above the ocean's surface is illustrated, along with the location of the top of the well-mixed layer η, shown by a dashed line, the lifting condensation level(s), shown as a blue shaded layer, the surface buoyancy flux $F_{b,s}$, and the processes that control the mass budget of the well-mixed layer (see equation (1)): the mass flux M, the entrainment rate at η, E and the large-scale vertical velocity at η, w_η. In (2) a scenario is illustrated whereby the mixed-layer q is perturbed by adding an amount of moisture δq. This lowers the surface energy input and the LCL, which in turn increases cloud (core) fraction and through equation (2) increases M. M removes moisture from the well-mixed layer and transports it upwards, thereby deepening the layer, which leads to additional downward mixing of drier free tropospheric air. In (3) the adjustment to a new equilibrium is shown, whereby larger M has led to a lowering of η (through equation (1)), bringing it close again to the LCL, thereby reducing cloud (core) fraction again.

increase the stability by increasing $\Delta_{TL} q$. Both processes lead to a reduction in the fraction of air parcels that saturate, which reduces M and brings the well-mixed layer to a new equilibrium state (Figure 8, # 3).

Note that a difference exists between the cloud core fraction a_c and the actual CF. CF is determined by all cloudy air parcels, including those that are negatively buoyant, whereas a_c only includes the fraction of positively buoyant parcels. LES indicates that values for CF are a factor 2–10 larger than a_c [*Siebesma et al.*, 2003; *VanZanten et al.*, 2011]. What might control differences between the two warrants further investigation, but at first order we may assume that the two are proportional and postulate that because convection acts to keep η and the LCL close to one another [*Albrecht et al.*, 1979], variations in CF$_{*LCL}$ are also limited.

Using this framework, it can be understood that the RH in the well-mixed layer can help regulate the LCL and thus CF$_{*LCL}$ on shorter-time scales. However, such local variations are poorly encapsulated in the RH averaged over a day or longer. Why we do not see a stronger relationship with RH on even shorter-time scales (not shown) is somewhat surprising, and in contrast with studies that have successfully linked humidity and temperature variations to cloudiness, most notably the work by [*Tompkins*, 2002] on statistical (PDF) cloud schemes. The temporal resolution of the measurements may play a role: although the updrafts and downdrafts are likely resolved, the larger humidity in the core of the updraft may not be. Furthermore, temperature fluctuations that matter to cloudiness on short-time scales are not resolved.

There appear to be mechanisms that may change CF$_{*LCL}$ on monthly time scales: namely, $d\theta/dz_{TL}$ has a negative relationship with CF$_{*LCL}$ and U_{L0} has a positive relationship with CF$_{*LCL}$. These relationships may be understood from equation (1) by noting that different equilibria ($\frac{d\eta}{dt} = 0$) are possible. Larger $d\theta/dz_{TL}$ may correspond to a smaller entrainment rate E and hence a smaller η, which would correspond to smaller a_c. As for the wind speed, which has appeared as an important factor in numerous studies [*Klein*, 1997; *Brueck et al.*, 2015], but generally receives less attention compared to thermodynamic arguments: an increase in U_{L0} linearly increases the surface buoyancy flux $F_{b,s}$. Energetically, the effect of larger $F_{b,s}$ is to increase the depth of the well-mixed layer η (through an increase in E): that deeper layer allows the vertical gradient of the buoyancy flux, which determines the local heating rate, to remain unchanged, in order to balance an unchanged radiative cooling rate [*Nuijens and Stevens*, 2012]. Thermodynamically, the effect of a larger wind speed is to lower the LCL. This is due to a decrease in the Bowen ratio and an increase in RH, due to a larger increase in the surface latent heat flux compared to the surface sensible flux, the latter being limited by the entrainment of relatively warm air [*Albrecht et al.*, 1979; *Betts and Ridgway*, 1989]. The increase in η through energetic constraints and the decrease in LCL through thermodynamic constraints would increase cloudiness. Other possibilities through which stronger winds may impact cloudiness are when they are accompanied by increased convergence, either locally, or when the ITCZ is located at higher latitudes in boreal summer (assuming that winds vanish at the ITCZ). Increased convergence would raise η by making w_h less negative. Stronger winds may also imply a larger wind shear, which would increase the projected cloud cover, although wind shear appeared a less important controlling factor than wind speed itself [*Brueck et al.*, 2015]. We also note that the anomaly profiles of u and v (Figure 4) do not suggest a strong role for shear. LES modeling studies would be necessary to better understand all these interactions.

4.2. Cloudiness Aloft
4.2.1. Observed and Modeled Seasonal Patterns
Large values of CF*$_{ALOFT}$ occur when numerous shallow cumuli near the LCL are accompanied by larger and deeper cumuli with stratiform layers near their tops [*Nuijens et al.*, 2014]. We have seen that stratiform cloud layers are more pronounced during the dry winter season (Figure 2, section 3.2). Therefore, the anomalous profiles during periods of large CF*$_{ALOFT}$ versus small CF*$_{ALOFT}$ (Figure 9) mainly reflect the dry and wet seasons. Months with larger CF*$_{ALOFT}$ are relatively drier and colder, experience large-scale subsidence, larger U_{L0} and larger wind shear. These months also have a notable trade-wind inversion between 800 and 700 hPa. Both *Klein* [1997], focusing on the stratocumulus-to-cumulus transition region, and *Brueck et al.* [2015], focusing on a region upstream of Barbados, found that low-level CC is best correlated with wind speed. Both studies also emphasize that the air mass history matters: air masses coming from colder, drier regions (under stronger subsidence) have larger lower tropospheric stability, which may promote low-level CC.

That said, the deeper clouds may occur during disturbed periods much shorter than a month, which deviate from the mean conditions during the dry season, a point which we return to in the next section.
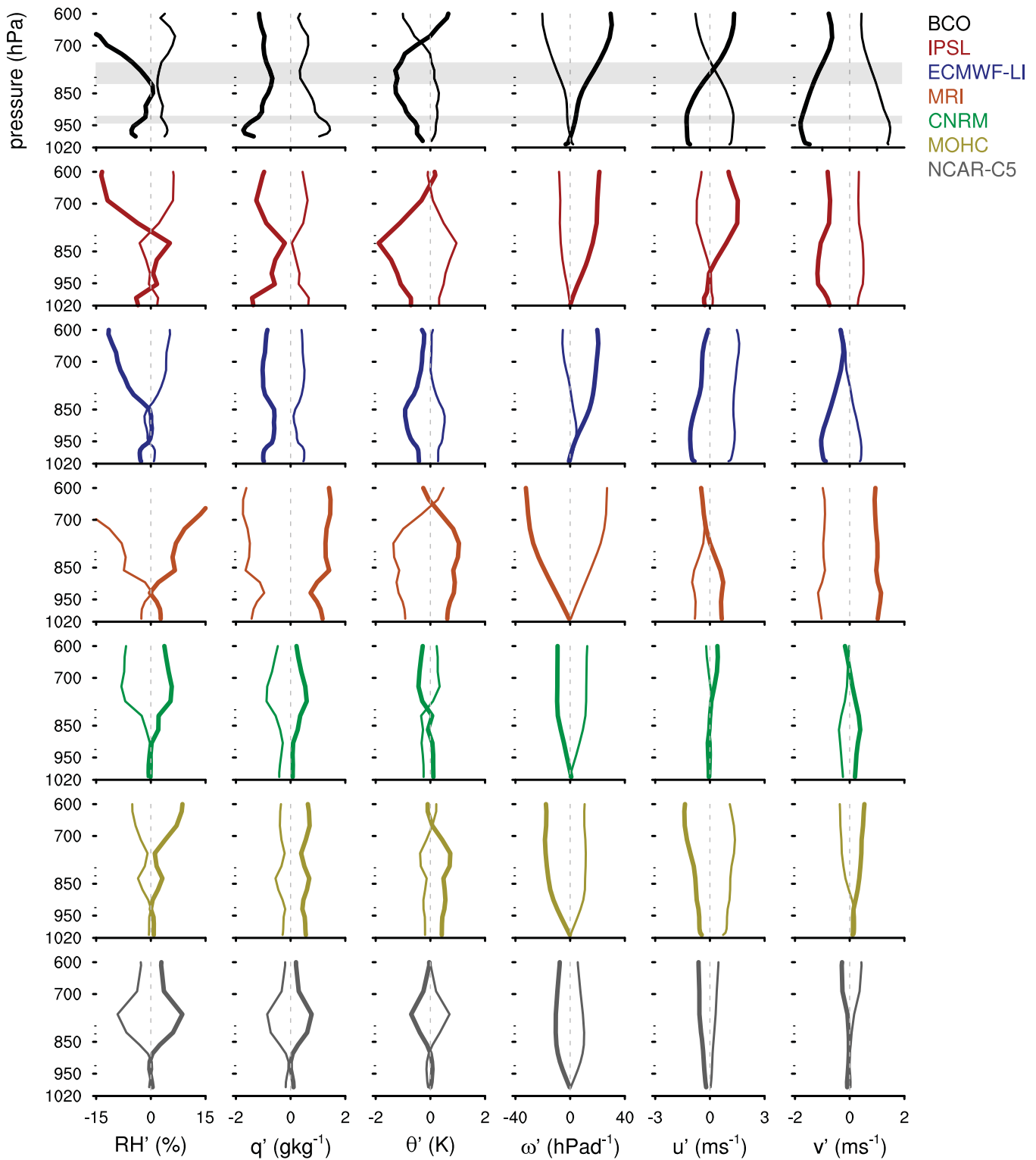
Figure 9. The anomalous thermodynamic and kinetic profiles for months with large CC_{ALOFT} (observations) or CF_{ALOFT} (models) (thick lines) and small values of CC_{ALOFT}, CF_{ALOFT} (thin lines). (top row) The observations; the following rows, models that frequently produce deeper cloud layers and for which large-scale parameters explain a larger fraction of variance in cloudiness aloft than they do in observations (R^2 (30d), Table 3).

The models in Figure 9 diverge in their patterns. Some models resemble the observations and have larger CF_{ALOFT} in the dry season (IPSL and ECMWF-LI) when the free troposphere is dry and warm and mean subsidence prevails. Other models show the opposite: larger CF_{ALOFT} is produced at times of mean ascent, when

Table 4. Similar to Table 3, but Then for the Variance Explained in CC_{ALOFT} (Observations) and CF_{ALOFT} (Models)[a]

Abbreviation	R^2 (1d)	X_s (1d)	r^2 (1d)	X_m (1d)	R^2 (30d)	X_s (30d)	r^2 (30d)	X_m (30d)
BCO	0.44	Δ_{CL} RH	0.28	Δ_{CL} RH	0.69	$\langle RH \rangle_{ML}$	0.42	$\Delta_{IL}\theta$
ECMWF-LI	0.39	Δ_{IL} RH	0.24	Δ_{CL} RH	0.79	Δ_{IL} RH	0.48	U_{L0}
MPIM-E63	0.19	Δ_{CL} RH	0.15	Δ_{CL} RH	0.46	Δ_{CL} RH	0.16	Δ_{CL} RH
MPIM-E62	0.05				0.10			
BCC	0.54	Δ_{CL} RH	0.31	Δ_{CL} RH	0.76	Δ_{CL} RH	0.49	Δ_{CL} RH
CCCma	0.11				0.47	Δ_{CL} RH	0.32	$\Delta_{IL}\theta$
IPSL	0.37	Δ_{IL} RH	0.26	Δ_{CL} RH	0.62	Δ_{IL} RH	0.60	U_{L0}
CNRM	0.45	ω_{825}	0.35	$\langle RH \rangle_{ML}$	0.66	ω_{825}	0.36	U_{L0}
MOHC	0.52	ω_{825}	0.43	Δ_{CL} RH	0.72	ω_{825}	0.36	Δ_{IL} RH
MRI	0.65	ω_{825}	0.43	Δ_{CL} RH	0.82	Δ_{CL} RH	0.64	Δ_{CL} RH
NCAR-C4	0.58	Δ_{CL} RH	0.29	Δ_{CL} RH	0.80	Δ_{IL} RH	0.48	Δ_{CL} RH
NCAR-C5	0.49	Δ_{CL} RH	0.28	Δ_{CL} RH	0.67	Δ_{IL} RH	0.50	Δ_{CL} RH

[a]The set of parameters used is the same, with one main difference, $d\theta/dz = \Delta_{IL}\theta$. For the observations and those models that produce clouds beyond 1 km often, the relationship of CC_{ALOFT}, CF_{ALOFT} with $d\theta/dz_{TL}$ is similar to that of CC_{LCL}, CF_{LCL} with $d\theta/dz_{TL}$.

the inversion is weaker and the lower troposphere is more humid (MRI, CNRM, MOHC, and NCAR-C5). During those months, the boundary layer overall appears to be much deeper and moister than what is typical for the trades.

Similar to what we did for CF_{LCL}, we next compare the regressions of CF_{ALOFT} with a set of predictors to discuss the most apparent relationships across time scales in the observations and the models.

4.2.2. Predictors of Cloudiness

On a day-to-day basis, CF^*_{ALOFT} varies more strongly with RH in the cloud layer (measured by Δ_{CL} RH, which scales mostly with RH_{825}) and with ω_{825} than what we have seen for CF^*_{LCL}. The fraction of variance explained by the selected set of predictors is also larger (0.44, compared to 0.24 for CF^*_{LCL}, Table 4). The stronger covariance can be explained because the main source of RH in the cloud layer is convection itself, which transports moisture out of the mixed-layer into the free troposphere. This relationship is already present on time scales of minutes (Figure 7b) and explains why the daily regression coefficient between CF^*_{ALOFT} and Δ_{CL} RH is relatively large at 0.5 (Figure 10).

Days with larger CF^*_{ALOFT} also correspond to weaker subsidence or larger mean ascent, so that the regression coefficient with ω_{825} is negative on daily time scales (Figure 10). This hints that synoptic disturbances, such as easterly waves, can promote CF^*_{ALOFT} even when on average that month experiences subsiding motion. Consistent with that relationship, the regression coefficient with Δ_{IL} RH is positive on daily time scales, reflecting a deepening and moistening of the cloud layer.
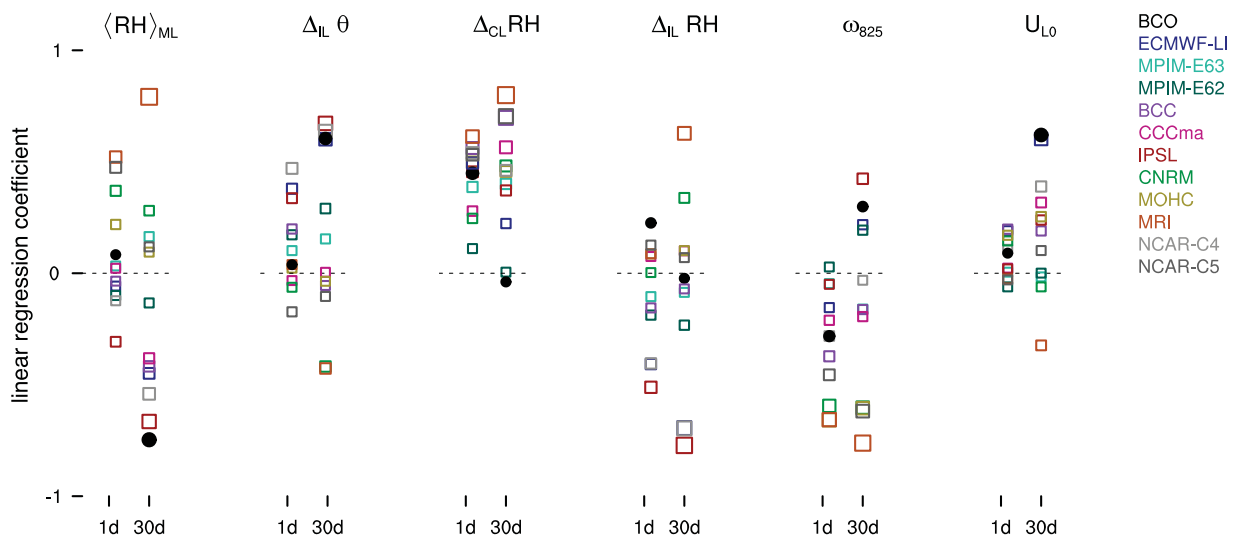

Figure 10. As in Figure 5, but then for the variance explained in CF_{ALOFT} (models) and CC_{ALOFT} (observations). The set of parameters used is the same with one main difference, $\Delta_{IL}\theta$ is used instead of $d\theta/dz_{TL}$.

Also on monthly time scales, the variance in CF*$_{ALOFT}$ is somewhat better explained by the selected set of predictors than the variance in CC$_{LCL}$. However, the covariance with Δ_{CL} RH (RH$_{825}$) is less pronounced, presumably because that covariance exists locally and is poorly encapsulated in longer averages. Parameters that do play an important role are $\Delta_{IL}\theta$ and U_{L0}. What may underlie these relationships is a greater potential for stratiform cloud layers to form under stronger inversions when surface evaporation is large [*Nuijens and Stevens*, 2012]. However, those conditions appear to be a prerequisite rather than a controlling factor, because neither covary strongly with CF*$_{ALOFT}$ on the shorter daily time scales.

The results suggest that an important factor for increasing CF*$_{ALOFT}$ and CC is the potential for trade-wind cumuli to deepen, but nevertheless maintain a limited depth so that the trade-wind layer structure is preserved. If the trade-wind inversion becomes less defined because much deeper convection transports moisture all the way through the cloud and inversion layers into the free troposphere, such as during the wet season (Figure 2, light grey line), CF$_{ALOFT}$ will decrease.

All models agree with the observations that days with larger Δ_{CL} RH and weaker subsidence correspond to larger CF$_{ALOFT}$ (Figure 10). Yet whereas such parameters become less important in the observations on monthly time scales or relationships between these parameters and CF$_{ALOFT}$ change sign, the majority of models continue to show strong relationships with Δ_{CL} RH and ω_{825}. Models disagree on the sign of the relationship with ω_{825}, which leads to opposing anomaly profiles (Figure 9). Some models produce the largest CF$_{ALOFT}$ in the wet season with strongest mean ascent (MRI, CNRM), whereas others reproduce the observations by producing the largest CF$_{ALOFT}$ in the dry season when strong inversions as well as stronger winds are present (ECMWF-LI, IPSL). Many models fail to reproduce the observed relationships with U_{L0} and $\Delta_{IL}\theta$, although a few models capture at least the relationship with $\Delta_{IL}\theta$ (BCC, IPSL, NCAR-C4) or with U_{L0} (ECMWF-LI).

5. Discussion

We have identified some common biases of global (climate) models in how they vary trade-wind cloudiness with the environment. First, models have stronger than observed relationships between CF$_{LCL}$ and the RH in the well-mixed layer. We explained that in nature, variations in RH may regulate the LCL and thus be linked to cloud formation locally, but that these local signatures diminish over longer-time scales. Furthermore, we explained how convection responds rapidly to perturbations in RH by ventilating the mixed-layer, which has a negative feedback on CF$_{LCL}$ (section 4.1.3). Apparently climate models do not represent such processes properly. Therefore, modeled CF$_{LCL}$ appears to be too sensitive to changes in RH.

Second, models have stronger than observed relationships between CF$_{LCL}$ and the temperature stratification at the top of the well-mixed layer. Models produce larger CF$_{LCL}$ when the transition layer and lower cloud layer are more stratified, whereas in observations larger cloudiness near the LCL is found when these layers are less stratified. Observations do show larger CF$_{ALOFT}$ underneath a stronger trade-wind inversion further aloft, which many models do not reproduce.

The models diverge in how they distribute CF and RH across the depth of the trade-wind layer. While some models reduce CF$_{LCL}$ as the RH in the cloud layer and CF$_{ALOFT}$ increase, other models keep CF$_{LCL}$ unchanged or even increase it.

We illustrate these different behaviors by means of Figures 11 and 12, which combine the behaviors of CF$_{LCL}$ and CF$_{ALOFT}$ seen in Figure 5 and 10. The plots in Figure 11 represent how parameters differ between days with a uniform distribution of moisture across the cloud layer and days with a less uniform distribution of moisture, whereby the latter is measured by Δ_{CL} RH. These differences, δ's, are derived as follows: we order all days by Δ_{CL} RH, from high to low values, and select the upper and lower quartiles of days. Because Δ_{CL} RH is generally negative, the upper quartile corresponds to small negative Δ_{CL} RH (well-mixed) and the lower quartile to large negative Δ_{CL} RH (larger gradients in RH throughout the cloud layer). $\delta \equiv \bar{\phi}_{upper} - \bar{\phi}_{lower}$ corresponds to the difference in a parameter ϕ between those two quartiles, whereby $\bar{\phi}_{upper}$ is the average ϕ over the upper quartile or days (and similar for the lower quartile). The grey-shaded box indicates negative δ's.

The range of values for $\delta(\Delta_{CL}RH)$ on the *x* axis (20–70%) illustrates that models have a much larger variance in RH gradients in the cloud layer than the observations suggest. Nevertheless, both observations and models agree that days with largest Δ_{CL} RH correspond to larger CF$_{ALOFT}$ and that the actual change in CF, which
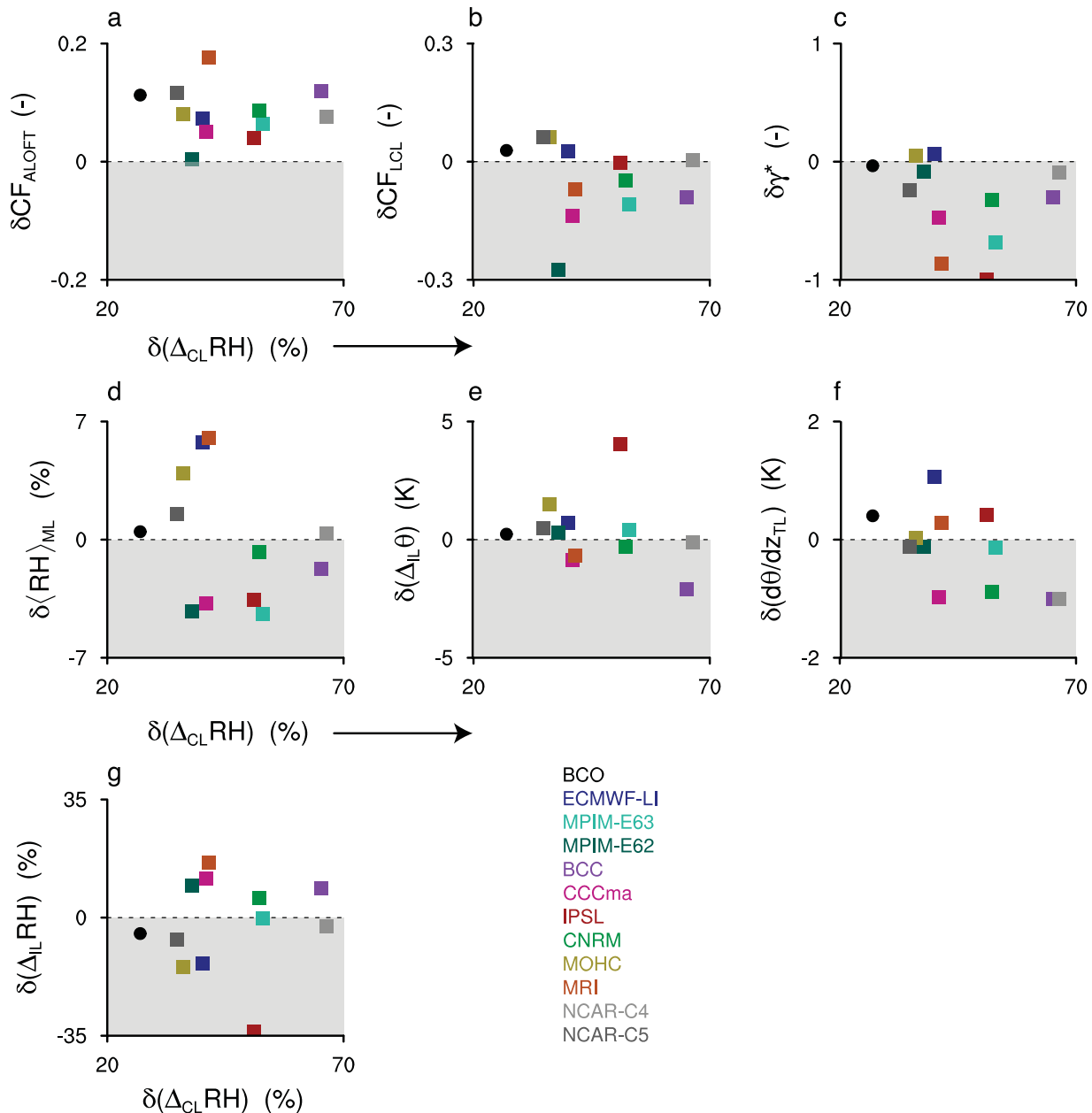
Figure 11. Each plot displays the difference (δ) in a parameter between days with a uniform distribution of moisture across the cloud layer and days with a less uniform distribution of moisture, as measured by $\Delta_{CL} RH = RH_{850}\text{-}RH_{LCL}$. δ is derived as follows: days are ordered by $\Delta_{CL} RH$ from high to low values. The difference between the upper and lower quartiles of days are taken: $\delta \equiv \bar{\phi}_{upper} - \bar{\phi}_{lower}$, whereby $\bar{\phi}_{upper}$ and $\bar{\phi}_{lower}$ are the average ϕ's over the upper, respectively, lower quartile of days. The selected parameters are: (a–g) CF_{ALOFT}, CF_{LCL}, $\gamma*$ (changes in the shape of the cloud profile, section 3.2), $\langle RH \rangle_{ML}$, $\Delta_{IL}\theta$, $d\theta/dz_{TL}$, and $\Delta_{IL} RH = RH_{700} - RH_{850}$. The grey-shaded box indicates negative δ's.

is less than 0.2, is modest (Figure 11a). In observations, those changes are accompanied by a small increase in CF_{LCL} (Figure 11b). A number of models instead show a large decrease in CF_{LCL} that falls into the grey-shaded area. These models have the largest decreases in $\gamma*$, which indicates that the models switch from bottom to top-heavy profiles ($\delta\gamma < 0$, (Figure 11c)), whereas in observations the CF profile becomes only slightly more top-heavy (remember also Figure 3). Because some of these models (MPIM-E62, CCCma) have large CF_{LCL} to begin with, and little to no CF_{ALOFT}, these changes can be quite effective at reducing low-level CC overall. The same models also show that the RH in the mixed-layer decreases ($\delta\langle RH \rangle_{ML} < 0$, Figure 11d) when the distribution of RH in the cloud layer becomes more uniform.

Brient et al. [2015] show that models that produce a bottom-heavy profile more effectively reduce cloudiness as climate warms and therefore have a high climate sensitivity. Our findings suggest that these models
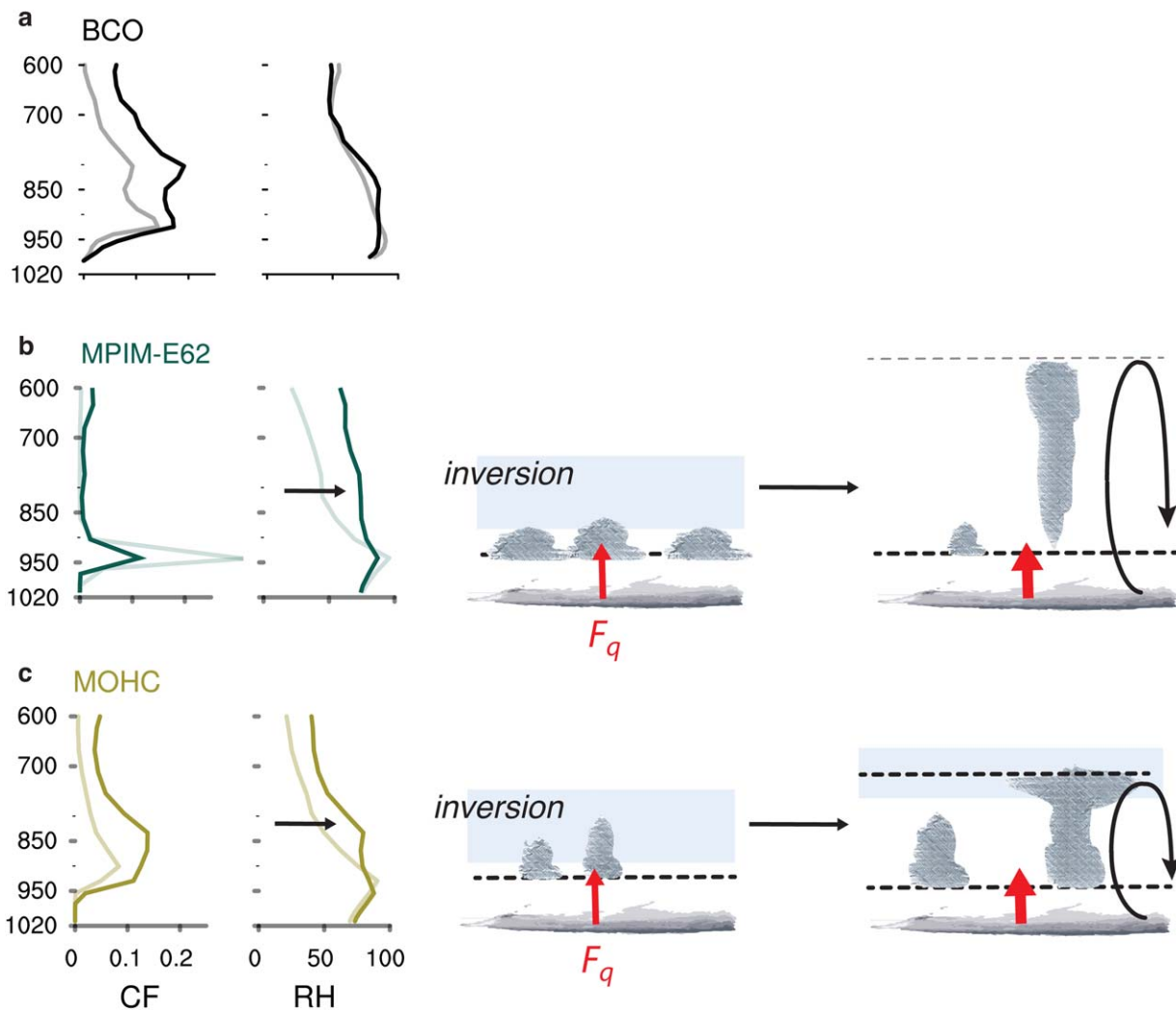
Figure 12. An illustration of different model behavior for a more uniform distribution of moisture across the cloud layer measured by Δ_{CL} RH (see also Figure 11). In this illustration, we imagine an increase in surface moisture flux (F_q) to trigger an increase in vertical moisture transport toward the upper cloud layer. Days are ordered by Δ_{CL} RH from high to low values. The modeled CF and RH profiles are averaged over the upper and lower quartiles of days and shown in dark, respectively, light solid lines. The BCO observations are shown as a reference at the top. The MPIM-E62 model is an example of a model that effectively reduces CF_{LCL} when moisture is mixed upward over a deep layer, whereby gradients and the inversion diminish. The MOHC model is an example of a model that increases CF_{LCL} along with CF_{ALOFT} as moisture is mixed upward, whereby the structure of the trade-wind layer and the inversion is maintained.

exhibit stronger relationships between CF and RH near the LCL than in observations. These models tend to shift cloud layers near the LCL to levels further aloft when moisture is mixed upward and the cumulus layer deepens, rather than sustaining cloudiness everywhere within the cumulus layer. The negative relationship between RH or CF near the inversion (850 hPa) and CF near the LCL is also apparent in a larger sample of CMIP models over all ocean regions that experience moderate subsidence or weak ascent *Medeiros and Nuijens* [2015].

Sherwood et al. [2014] furthermore show that the simulated vertical moisture structure over tropical oceans in present-day climate separates high from low climate sensitivity models. They use Δ_{IL} RH as a measure of lower tropospheric mixing and relate models with a small Δ_{IL} RH to a high climate sensitivity. By diagnosing Δ_{IL} RH only over the western Pacific warm pool, where mean ascent dominates, they ensure that convection is indeed the lead effect on moisture at those levels, rather than variations in large-scale descent. They then argue that those models that sustain small Δ_{IL} RH are apparently very effective at mixing moisture all the way from the well-mixed layer to the free troposphere (700 hPa). Presumably, as this mixing increases with global mean temperature CF_{LCL} disappears.

We find that models that are effective at mixing moisture by the definition of *Sherwood et al.* [2014] are indeed those that readily dissipate clouds near the LCL in the present-day climate. These are the models in

Figure 11 that reduce temperature and moisture gradients throughout the lower troposphere as they reduce CF_{LCL}. An illustration of this behavior using the MPIM-E62 model as an example is shown in Figure 12b. The potential temperature difference across the inversion layer decreases ($\delta \Delta_{IL} \theta < 0$) and so does the temperature stratification across the transition layer ($\delta \Delta_{TL} \theta < 0$). Furthermore, the RH difference across the inversion layer decreases ($\delta \Delta_{IL} RH > 0$, because $\Delta_{IL} RH$ becomes less negative).

This behavior contrasts with other models, which distribute RH and CF more uniformly across the cloud layer, so that as CF_{ALOFT} increases, CF_{LCL} changes little or increases by a small amount (MOHC, NCAR-C5, ECMWF-LI). The MOHC model is used to illustrate this behavior (Figure 12c). These models tend to maintain the structure of the trade-wind layer, in terms of layers separated by gradients. The associated larger temperature stratification in the transition layer in these models ($\delta\, d\theta/dz_{TL} > 0$) may provide an additional mechanism through which moisture is capped within the well-mixed layer, which sustains cloud layers there. On the other hand, these models have a much stronger than observed positive relationship between CF_{LCL} and large-scale ascent (Figure 5). Of the models that we have analyzed here, the BCC, NCAR-C4, and MRI models have a low climate sensitivity in *Sherwood et al.* [2014]. In turn, high climate sensitivity models in *Sherwood et al.* [2014] include the MPIM-E62, IPSL, CCCma, and CNRM models.

In observations, neither a large decrease nor a large increase in CF_{LCL} is evident when large-scale vertical motion or RH in the cloud layer changes. However, it would be easy to misjudge a model's behavior as being more realistic, and therefore its climate sensitivity as more trustworthy, by means of a single process such as vertical moisture mixing. There is no model that stands out by reproducing observed relationships in all respects. The climate models that we have analyzed here for instance lack either constraints on CF_{LCL} due to convection, a sensitivity to wind speed and the strength of the trade-wind inversion, or an insensitivity to large-scale vertical velocity on longer-time scales. Because changes in cloudiness will be a combined response to changes in a variety of factors [see also *Bretherton et al.*, 2013], many of which are connected through circulations and some of which are regulated by convection itself, a better understanding of the role of large-scale circulations versus the role of convection deserves more attention.

6. Summary and Conclusions

We evaluated global (climate) models for their ability to reproduce observed patterns of covariability between the structure of the trade-wind layer, cloudiness, and the thermodynamic and kinetic environment. A ground-based measurement site established on the Island of Barbados has provided the data required to study such variability in detail. We used these measurements for a period of up to 4 years and compared them to multiyear single-time step output from models at a single site near or upstream of Barbados. The models include a subset of CMIP5 models and the ECMWF Integrated Forecast System; we ran the latter in a climate-model-like long integration mode.

All the models exhibit the basic observed features of a trade-wind layer. Specifically, models produce a well-mixed layer approximately 500–1000 m deep throughout which RH increases, peaking at cloud base at a value less than 100%. Accordingly, CF is on average smaller than 0.4 throughout the cloud layer. The location of the trade-wind inversion in both observations and models ranges from 850 hPa ($\approx$2 km) to 600 hPa ($\approx$4 km), reflecting the ability of trade-wind cumuli to reach substantial depth. As the ITCZ migrates northward in boreal summer and vertical motion at Barbados changes from mean descent to mean ascent, temperatures increase throughout the column and RH increases above the trade-wind layer. Corresponding changes in the CF profile are relatively small, which the majority of models reproduce.

However, when moving away from long-term means and looking at variability instead, it is evident that models achieve their fairly realistic climatology through rather unrealistic variability on shorter-time scales. This raises an important question, namely whether models can capture potential changes in trade-wind cloudiness in a warmer climate.

Variability in cloudiness is analyzed at two important height levels: (1) near the lifting condensation level (LCL) or cloud base (CF_{LCL}), and (2) near the detrainment level (cloud tops) of the deepest cumuli at the trade-wind inversion (CF_{ALOFT}). CF_{LCL} is important because it contributes on average two-thirds to low-level cloud cover and is relatively invariant when averaged over a few days or longer. Relationships between CF_{LCL} and RH, or other measures of the trade-wind layer structure, are weak. We explained that a negative

feedback of cumulus convection on CF_{LCL}, which can be found in theoretical models of convection, appears present in the observations. In this negative feedback, cumulus convection acts like a valve on top of the well-mixed layer that removes mass as soon as cloud formation is abundant. This mechanism maintains the height of the mixed-layer top in the vicinity of the LCL, which in turn constraints CF.

CF_{ALOFT} on the other hand is important because it contributes most to the variance in low-level cloud cover. CF at this level covaries with the strength of the trade-wind inversion and with surface wind speed on monthly time scales, leading to larger CF_{ALOFT} in boreal winter, when the trade winds are stronger and lower tropospheric stability is larger. However, variance in CF_{ALOFT} on shorter daily time scales is unexplained by these factors.

None of the models that we analyzed stands out by reproducing the observations better in all respects. Almost all models overestimate the variance in CF_{LCL} compared to the variance in CF_{ALOFT} on shorter (daily) timescales. The large variance in modeled CF_{LCL} lies in stronger than observed relationships between CF_{LCL} and RH in the well-mixed layer. Furthermore, whereas in nature modest decreases in CF_{LCL} are observed when the temperature stratification in the transition layer is larger (and convection is limited), the models show larger CF_{LCL} under such conditions instead.

Most models do not indicate that the strength of the inversion and the surface wind speed can promote CF_{ALOFT} in boreal winter. Models diverge in how they distribute CF and RH vertically across the trade-wind layer and in particular in response to changes in large-scale vertical motion. One group of models places most cloud layers near the LCL in a shallow layer with large CF. Cloud layers aloft are produced when moisture is transported away from the surface to levels near and above the inversion. This dries the mixed-layer and lower part of the cloud layer at the expense of CF_{LCL}. A very bottom-heavy profile (no CF_{ALOFT}) is then exchanged for a very top-heavy profile (no CF_{LCL}). These models behave like the ones that *Sherwood et al.* [2014] refers to as models with a large vertical mixing potential, which effectively dry the mixed layer and cloud layer when climate warms. These models appear to reduce cloudiness, especially near the LCL, too eagerly when vertical mixing increases. Another group of models distributes RH and CF more uniformly across the cloud layer, so that CF near the LCL is maintained when moisture is mixed upwards and CF aloft increases. However, this increase is strongly linked to periods of mean ascent, which is unsupported by the observations.

Modeled cloud changes in present-day climate thus appear to have a larger susceptibility to changes in their environment than the observations. This highlights that cloudiness in models is not entirely regulated by the processes that underlie variations in cloudiness in nature, which decreases our confidence that climate models can realistically predict the response of trade-wind clouds to increasing global temperatures.

References

Albrecht, B., A. Betts, W. Schubert, and S. Cox (1979), A model of the thermodynamic structure of the trade-wind boundary layer. part i: Theoretical formulation and sensitivity tests, *J. Atmos. Sci.*, *36*, 73–89.

Betts, A., and W. Ridgway (1989), Climatic equilibrium of the atmospheric convective boundary layer over a tropical ocean, *J. Atmos. Sci.*, *46*, 2621–2641.

Bony, S., and J.-L. Dufresne (2005), Marine boundary layer clouds at the heart of tropical cloud feedback uncertainties in climate models, *Geophys. Res. Lett.*, *32*, L20806, doi:10.1029/2005GL023851.

Bony, S., and K. A. Emanuel (2001), A parameterization of the cloudiness associated with cumulus convection; evaluation using TOGA COARE data, *J. Atmos. Sci.*, *58*, 3158–3183.

Bretherton, C. S., P. N. Blossey, and C. R. Jones (2013), Mechanisms of marine low cloud sensitivity to idealized climate perturbations: A single-LES exploration extending the CGILS cases, *J. Adv. Model. Earth Syst.*, *5*, 316–337, doi:10.1002/jame.20019.

Brient, F., T. Schneider, Z. Tan, S. Bony, X. Qu, and A. Hall (2015), Shallowness of tropical low clouds as a predictor of climate models' response to warming, *Clim. Dyn.*, 1–17, doi:10.1007/s00382-015-2846-0.

Brueck, H. M., L. Nuijens, and B. Stevens (2015), On the seasonal and synoptic timescale variability in low level cloudiness in the North Atlantic trades, *J. Atmos. Sci.*, *72*, 1428–1446.

Carlson, T. N., and J. M. Prospero (1972), The large-scale movement of Saharan air outbreaks over the northern equatorial Atlantic, *J. Appl. Meteorol.*, *11*(2), 283–297, doi:10.1175/1520-0450(1972)011<0283:TLSMOS>2.0.CO;2.

Emanuel, K. (1993), A cumulus representation based on the episodic mixing model: The importance of mixing and microphysics in predicting humidity, in *The representation of Cumulus Convection in Numerical Models. Meteorological Monographs*, vol. 24, edited by K. Emanuel and D. J. Raymond, chap. 19, pp. 185–194, Am. Meteorol. Soc., Boston.

Fletcher, J. K., and C. S. Bretherton (2010), Evaluating boundary layer-based mass flux closures using cloud-resolving model simulations of deep convection, *J. Atmos. Sci.*, *67*(7), 2212–2225, doi:10.1175/2010JAS3328.1.

Gettelman, A., et al. (2010), Multi-model assessment of the upper troposphere and lower stratosphere: Tropics and global trends, *J. Geophys. Res.*, *115*, D00M08, doi:10.1029/2009JD013638.

Gregory, D., and P. R. Rowntree (1990), A mass flux convection scheme with representation of cloud ensemble characteristics and stability-dependent closure, *Mon. Weather Rev.*, *118*(7), 1483–1506, doi:10.1175/1520-0493(1990)118<1483:AMFCSW>2.0.CO;2.

Klein, S. A. (1997), Synoptic variability of low-cloud properties and meteorological parameters in the subtropical trade wind boundary layer, *J. Clim.*, *10*, 2018–2039.

Klein, S. A., and D. L. Hartmann (1993), The seasonal cycle of low stratiform clouds, *J. Clim.*, *6*, 1587–1606.

Lock, A. P. (2009), Factors influencing cloud area at the capping inversion for shallow cumulus clouds, *Q. J. R. Meteorol. Soc.*, *952*, 941–952, doi:10.1002/qj.424.

Malkus, J. S. (1958), On the structure of the trade wind moist layer, *Pap. Phys. Oceanogr. Meteorol.*, *13*(2), 1–47.

McFarlane, N., J. F. Scinocca, M. Lazare, R. Harvey, D. Verseghy, and J. Li (2005), The CCCma third generation atmospheric general circulation model (AGCM3), CCCma internal report, 25 pp., Can. Cent. for Clim. Modell. and Anal., 25 pp., Univ. of Victoria.

Medeiros, B., and L. Nuijens (2015), Barbados and Beyond: Trade-wind cloud regimes in observations and climate models, *Proc. Natl. Acad. Sci.*, U. S. A.

Medeiros, B., and B. Stevens (2011), Revealing differences in GCM representations of low clouds, *Clim. Dyn.*, *36*, 385–399.

Medeiros, B., C. Antoniazzi, L. Nuijens, and B. Stevens (2010), Low-latitude boundary layer clouds as seen by CALIPSO, *J. Geophys. Res.*, *115*, D23207, doi:10.1029/2010JD014437.

Neggers, R., B. Stevens, and J. D. Neelin (2006), A simple equilibrium model for shallow-cumulus-topped mixed layers, *Theor. Comput. Fluid Dyn.*, *20*(5-6), 305–322, doi:10.1007/s00162-006-0030-1.

Neggers, R. A. J., and A. P. Siebesma (2013), Constraining a system of interacting parameterizations through multiple-parameter evaluation: Tracing a compensating error between cloud vertical structure and cloud overlap, *J. Clim.*, *26*(17), 6698–6715, doi:10.1175/JCLI-D-12-00779.1.

Neggers, R. a. j., a. P. Siebesma, and T. Heus (2012), Continuous single-column model evaluation at a permanent meteorological supersite, *Bull. Am. Meteorol. Soc.*, *93*(9), 1389–1400, doi:10.1175/BAMS-D-11-00162.1.

Nuijens, L., and B. Stevens (2012), The influence of wind speed on shallow marine cumulus convection, *J. Atmos. Sci.*, *69*(1), 168–184, doi:10.1175/JAS-D-11-02.1.

Nuijens, L., I. Serikov, L. Hirsch, K. Lonitz, and B. Stevens (2014), The distribution and variability of low-level cloud in the North Atlantic trades, *Q. J. R. Meteorol. Soc.*, *140*, 2364–2374, doi:10.1002/qj.2307.

Nuijens, L., B. Medeiros, I. Sandu, and M. Ahlgrimm (2015), The behavior of trade-wind cloudiness in models and observations: The major cloud components and their variability, *J. Adv. Model. Earth Syst.*, *7*, 600–616, doi:10.1002/2014MS000390.

Phillips, T. J., G. L. Potter, D. L. Williamson, R. T. Cederwall, J. S. Boyle, M. Fiorino, J. J. Hnilo, J. G. Olson, S. Xie, and J. J. Yio (2004), Evaluating parameterizations in general circulation models: Climate simulation meets weather prediction, *Bull. Am. Meteorol. Soc.*, *85*(12), 1903–1915, doi:10.1175/BAMS-85-12-1903.

Qu, X., A. Hall, S. Klein, and P. Caldwell (2014), On the spread of changes in marine low cloud cover in climate model simulations of the 21st century, *Clim. Dyn.*, *42*(9-10), 2603–2626, doi:10.1007/s00382-013-1945-z.

Rasch, P. J., and J. E. Kristjansson (1998), A comparison of the CCM3 model climate using diagnosed and predicted condensate parameterizations, *J. Clim.*, *11*, 1587–1614.

Ricard, J. L., and J. F. Royer (1993), A statistical cloud scheme for use in an AGCM, *Ann. Geophys.*, *11*, 1095–1115.

Serikov, I., and S. Bobrovnikov (2010), Atmospheric temperature profiling with pure rotational Raman lidars, in *Recent Advances in Atmospheric Lidars*, edited by L. Fiorani and V. Mitev, Optoelectronic materials and devices, vol. 7, pp. 149–216, INOE (INTEGRA NATURA OMNIA ET AETERNA), Rom.

Sherwood, S. C., S. Bony, and J.-L. Dufresne (2014), Spread in model climate sensitivity traced to atmospheric convective mixing, *Nature*, *505*(7481), 37–42, doi:10.1038/nature12829.

Siebesma, A. P., et al. (2003), A large eddy simulation intercomparison study of shallow cumulus convection, *J. Atmos. Sci.*, *60*(10), 1201–1219, doi:10.1175/1520-0469(2003)60<1201:ALESIS>2.0.CO;2.

Simmons, A., S. Uppala, D. Dee, and S. Kobayashi (2007), Era-interim: New ECMWF reanalysis products from 1989 onwards, *ECMWF Newslett.*, *110*, 25–35.

Slingo, J. M. (1980), A cloud parametrization scheme derived from GATE data for use with a numerical model, *Q. J. R. Meteorol. Soc.*, *106*, 747–770.

Slingo, J. M. (1987), The development and verification of a cloud prediction scheme for the ECMWF model, *Q. J. R. Meteorol. Soc.*, *113*, 899–927.

Stevens, B. (2006), Bulk boundary-layer concepts for simplified models of tropical dynamics, *Theor. Comput. Fluid Dyn.*, *20*(5-6), 279–304, doi:10.1007/s00162-006-0032-z.

Stevens, B., et al. (2001), Simulations of trade wind cumuli under a strong inversion, *J. Atmos. Sci.*, *58*(14), 1870–1891.

Stevens, B., et al. (2015), The Barbados Cloud Observatory – Anchoring investigations of clouds and circulation on the edge of the ITCZ, *Bull. Am. Meteorol. Soc.*, in press.

Sundqvist, H., E. Berge, and J. E. Kristjansson (1989), Condensation and cloud parameterization studies with a mesoscale numerical weather prediction model, *Mon. Weather Rev.*, *117*, 1641–1657.

Tiedtke, M. (1989), A comprehensive mass flux scheme for cumulus parameterization in large-scale models, *Mon. Weather Rev.*, *117*, 1779–1800.

Tiedtke, M. (1993), Representation of clouds in large-scale models, *Mon. Weather Rev.*, *121*, 3040–3061.

Tompkins, A. M. (2002), A prognostic parameterization for the subgrid-scale variability of water vapor and clouds in large-scale models and its use to diagnose cloud cover, *J. Atmos. Sci*, *59*(12), 1917–1942.

VanZanten, M. C., et al. (2011), Controls on precipitation and cloudiness in simulations of trade-wind cumulus as observed during RICO, *J. Adv. Model. Earth Syst.*, *3*, M06001, doi:10.1029/2011MS000056.

Vial, J., J. L. Dufresne, and S. Bony (2013), On the interpretation of inter-model spread in CMIP5 climate sensitivity estimates, *Clim. Dyn.*, *41*, 3339–3362, doi:10.1007/s00382-013-1725-9.

von Salzen, K., N. McFarlane, and M. Lazare (2005), The role of shallow convection in the water and energy cycles of the atmosphere, *Clim. Dyn.*, *25*(7-8), 671–688, doi:10.1007/s00382-005-0051-2.

Webb, M et al. (2015), The diurnal cycle of marine cloud feedback in climate models, *Clim. Dyn.*, *44*(5-6), 1419–1436, doi:10.1007/s00382-014-2234-1.

Wu, T., R. Yu, F. Zhang, Z. Wang, M. Dong, L. Wang, X. Jin, D. Chen, and L. Li (2010), The Beijing Climate Center atmospheric general circulation model: Description and its performance for the present-day climate, *Clim. Dyn.*, *34*(1), 123–147, doi:10.1007/s00382-008-0487-2.

Yukimoto, S., et al. (2012), A new global climate model of the meteorological research institute: Mri-cgcm3 model description and basic performance, *J. Meteorol. Soc. Jpn.*, *90A*, 23–64, doi:10.2151/jmsj.2012-A02.

Zhang, G. J., and N. A. McFarlane (1995), Sensitivity of climate simulations to the parameterization of cumulus convection in the Canadian climate centre general circulation model, *Atmos. Ocean*, *33*(3), 407–446, doi:10.1080/07055900.1995.9649539.